Investigation of Novel Properties in Ludwigites

A thesis submitted towards partial fulfilment of
BS-MS Dual Degree Programme

by

Deepak John M

under the guidance of

Dr. Sunil Nair
Assistant Professor

Indian Institute of Science Education and Research, Pune

Certificate

This is to certify that this thesis entitled ***Investigation of Novel Properties in Ludwigites*** submitted towards the partial fulfillment of the BS-MS dual degree programme at the Indian Institute of Science Education and Research, Pune represents original research carried out by **Deepak John M** at Indian Institute of Science Education and Research, Pune, under the supervision of **Dr. Sunil Nair** during the academic year 2015 - 2016.

Student
Deepak John M

Supervisor
Dr. Sunil Nair

Declaration

I hereby declare that the matter embodied in the report entitled ***Investigation of Novel Properties in Ludwigites*** are the results of the investigations carried out by me at the Department of Physics, Indian Institute of Science Education and Research, Pune, under the supervision of Dr. Sunil Nair and the same has not been submitted elsewhere for any other degree.

Student
Deepak John M

Supervisor
Dr. Sunil Nair

Acknowledgments

I would like to thank Dr. Sunil Nair for his constant support and guidance for the past three years and especially during my fifth year. His enthusiasm and passion towards science has encouraged me during the past years. Constant discussions with him has helped me in crisis and also enriched my knowledge. I would like to thank Dr. Jitender Thakur for this support during the project and for the ideas he contributed to this work. He was the one I turned towards for help in all matters especially in analyzing data and getting results from different sources. The support and help of my lab members for the past three years was very helpful. Soumendra Panja, Sarath Thadeti, Avirup De, Charu Garg, Rohit Kumar, Shruti Chakravarty, Kaustav Dey and Devika T.D who were like family members to me in IISER. The time I spent with my lab members in and out of lab were memorable. I would like to extent my gratitude towards Dr. Surjeeth Singh, who was my TAC member, and his lab members mainly Prachi Telang, Rabindranath Bag and Giri M. Also for letting me use PPMS for my samples specific heat measurements. Special thanks to TIFR were some of my specific heat and dielectric measurements were being carried out. To my best friends in IISER particularly to Akshay, Asmi, Sohan and Charu who constantly supported me. Finally to my dearest family members who believed in me and prayed for the success of this work and for my future.

Abstract

Ludwigites are a class of oxyborates with the chemical formula $M_2(II)M'(III)O_2BO_3$ where M and M' are metal ions. These materials have been widely studied because of its three leg ladder structure and spin and charge ordering along these triads. Due to their interesting properties like charge ordering and weak ferromagnetism, they are also potential candidates for multiferroicity. This project aims to investigate the structural, magnetic, dielectric and specific heat properties of some newly synthesized ludwigite systems. During this project two of the rarely studied ludwigites $Ni_2AlO_2BO_3$ and $Co_2AlO_2BO_3$ were synthesized using flux growth, with borax as the flux. Both of these compounds have orthorhombic crystal structure, with space group symmetry *Pbam*. Magnetic measurements showed antiferromagnetic ordering at 38K and 36K for $Ni_2AlO_2BO_3$ and $Co_2AlO_2BO_3$ respectively. There also appears to be a first order transition in $Co_2AlO_2BO_3$ at 50K. Magnetization and specific heat vs. Field measurements at different temperatures showed metamagnetic transitions for both of these samples. The possibility of magnetodielectric effect has been observed in dielectric measurements done for $Ni_2AlO_2BO_3$ which is indicated by a sharp jump in the dielectric constant at the magnetic transition temperature. Specific heat measurements showed large magnetocaloric effect (MCE) in both $Ni_2AlO_2BO_3$ and $Co_2AlO_2BO_3$ with MCE in $Co_2AlO_2BO_3$ being two times higher than that in $Ni_2AlO_2BO_3$.

Contents

List of Figures

List of Tables

Chapter 1

Introduction

1.1 Ludwigites

During the past few decades, compounds with ludwigite crystal structures have been widely studied for its interesting magnetic and structural properties. Some of the main reasons for these properties are, its disorder in site occupancy, valence fluctuations of metal ions and more importantly a three leg ladder structure exhibited by transition metal ions in these compounds. This project aims to explore some of the properties of alumino-ludwigites. Ludwigites belong to a general class of boron containing compounds called oxyborates. Anhydrous borates, with boron ions present in trigonal coordination in orthoborate group $(BO_3)^{3-}$, with at least one oxygen ion not directly bonded to the orthoborate group are called oxyborates [1]. There are different classes of oxyborates depending upon the structural features of the material. Some of the common examples are warwickites and ludwigites. Each class of oxyborate posses one special structural feature which distinguishes it from one another.

Ludwigites are named after the Austrian scientist Ernst Ludwig (1842–1915) who first described a mineral $Mg_2FeO_2BO_3$ in 1874. Ludwigites in general have a chemical formula $(M_2(II)M'(III)O_2)^{3+}(BO_3)^{3-}$ where M and M' are metal ions. These systems have orthorhombic crystal structure with metal ions in the center of a distorted oxygen octahedra and are mostly found in *Pbam* space group with some rare exceptions [1].

Depending upon the type of metal ions present, these class of materials can be divided into two groups : the homometallic ludwigites and the hetrometallic ludwigites. As the name suggests, in homometallic ludwigites there is only one type of metal ion, so the same metal ion species takes two different oxidation states +3 and +2. In most of the metals, one of the oxidation state is favored more than the others, thus reducing the homometallic ludwigites to only two : $Fe_2(II)Fe(III)O_2BO_3$ and $Co_2(II)Co(III)O_2BO_3$. In hetrometallic ludwigites M and M' are not the same ions, thus giving rise to a wide range of compounds. Some of the hetrometallic ludwigites are $Cu_2FeO_2BO_3$, $Ni_2FeO_2BO_3$, $Cu_2AlO_2BO_3$, $Co_2FeO_2BO_3$, $Mg_2FeO_2BO_3$ and so on.

[1] The exception is for $Cu_2FeO_2BO_3$ due to Jahn Teller distortion, symmetry of is reduced giving a monoclinic structure with space group $P2_1/c$ [2].

1.1.1 Structural Properties of Ludwigites

As mentioned above, every oxyborate has some special structural feature which makes it unique from others. In the case of ludwigites, there is zig-zag wall which propagates along the crystallographic c direction. Figure 1.1 shows a general structure of ludwigite projected to (001) crystallographic plane, where we can see zig-zag walls. These zig-zag walls are made of edge sharing oxygen octahedra, and is unique to the structure of ludwigites.

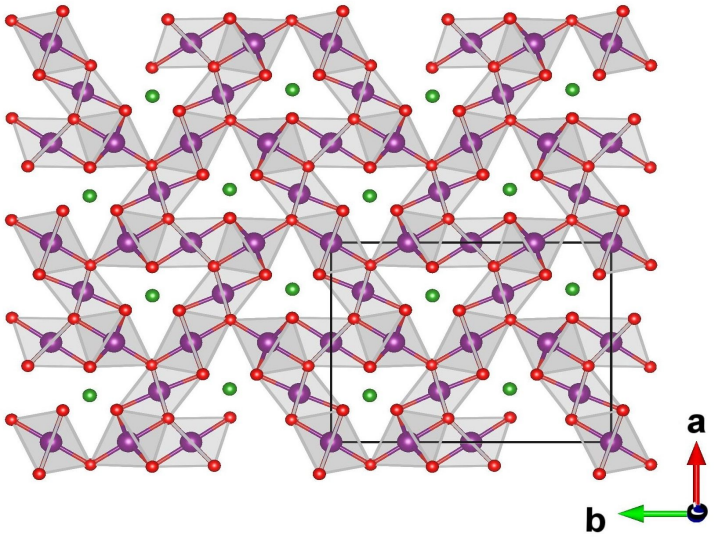

Figure 1.1: Crystal structure of ludwigite projected along (001) direction showing zig-zag walls formed by edge sharing oxygen octahedra. Red, green and purple atoms are oxygen, boron and metal ions respectively. Black line shows the boundary of a single unit cell

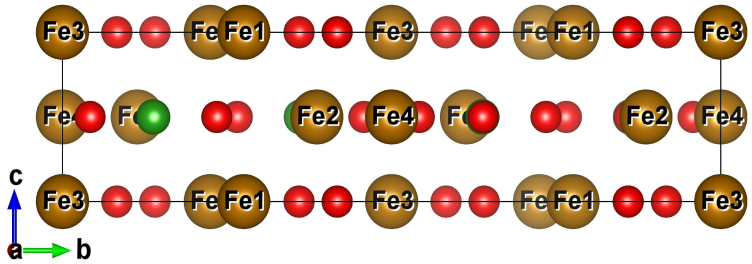

Figure 1.2: Crystal structure of $Fe_3O_2BO_3$ projected along crystallographic a direction showing different crystallographic metal ion sites. Red, brown and green atoms are oxygen, metal ion and boron respectively. Metal ion planes are visible and are separated by 1.5$\mathring{A}$ in the c direction.

Since metal ions are inside distorted oxygen octahedra, structure of ludwigites dictates that there should be four non equivalent crystallographic metal ion positions as

shown in figure 1.2. Metal ions at sites 3 and 4 are twice the number of metal ion positions 1 and 2. Each of these metal ions from a plane with respect to the c direction. Metal ions 1 and 3 from a plane which is parallel to the plane formed by metal ions 2 and 4. These planes are apart by a distance of one half the lattice parameter in crystallographic c direction, which is approximately 1.5Å. The BO_3 group lies in the plane of metal ions 2 and 4. Figure 1.2 shows the metal ion planes in $Fe_3O_2BO_3$ when projected along the crystallographic a direction. It can be seen from the figure that metal ion planes are apart by half the value of lattice parameter c.

There are three characteristic bond distances present, with the shortest being the one between B and O, which is ionic in nature and thus the strongest. The second is metal ion distance which is of the order of 3Å. The third is metal ion and oxygen bond length, which is of the order of 2Å. The different bonds in ludwigites are shown in figure 1.3. It has been observed that the metal ion oxygen bonds are similar for all the four crystallographic positions [3].

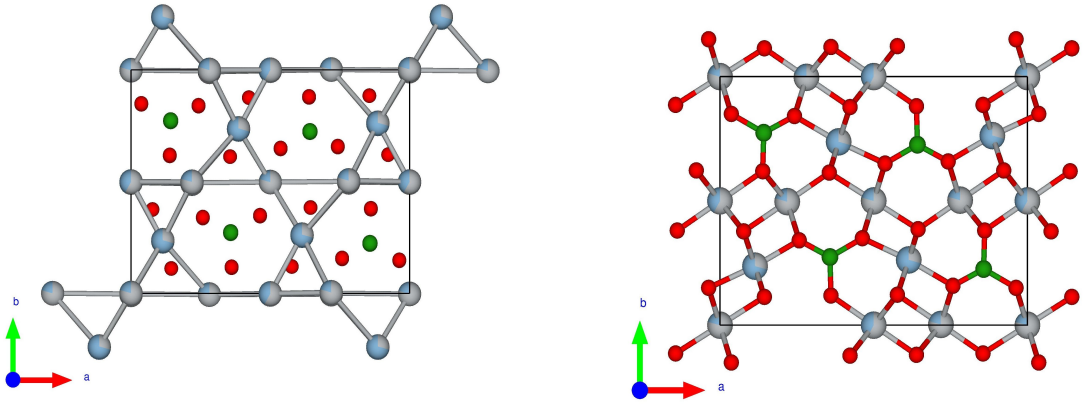

(a) (b)

Figure 1.3: Bond distances present in Ludwigites projected in (001) direction (a) Grey bonds are metal ion distances $\approx 3\mathring{A}$ (b) Grey red bonds are metal ion bond with oxygen atoms $\approx 2\mathring{A}$ and red green bonds are bonds with oxygen and boron atoms $\approx$ 1.3Å[3].

Each ludwigite system shows interesting structural and magnetic properties and there are a number of ludwigites known to us. Since it is not in the scope of this thesis to give an introduction to all of the ludwigites, we will concentrate on two ludwigite compounds : the homometallic $Fe_3O_2BO_3$ and the hetrometallic $Co_{2.4}Ga_{0.6}O_2BO_3$. The hetrometallic ludwigite $Co_{2.4}Ga_{0.6}O_2BO_3$ closely resembles in chemical composition of $Co_2AlO_2BO_3$ which is one of the compounds studied in detail in this project.

1.1.2 A Homometallic ludwigite: $Fe_3O_2BO_3$

Homometallic ludwigites have been extensively studied during the past decade. Especially $Fe_3O_2BO_3$, which shows a structural transition around 283 K followed by two

magnetic transitions at lower temperatures [4]. $Fe_3O_2BO_3$ shows an antiferromagnetic transition at 112 K followed by a ferromagnetic transition at 70 K and below 40 K shows weak ferromagnetism [5]. This Ludwigite is mainly known for its three leg ladders (triads) Fe4-Fe2-Fe4 where strong exchange interactions are present along the rungs of ladder and along the ladder. Symmetric high charge state resides along the central rung of the ladder.

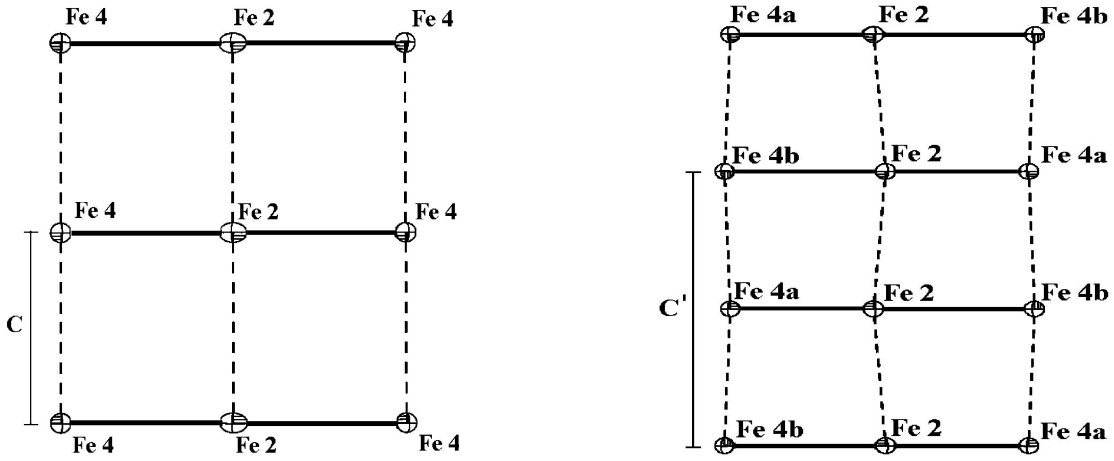

Figure 1.4: Three leg ladders (triads) in $Fe_3O_2BO_3$, (a) Triads above structural transition temperature (283K) at 294 K (b) below structural transition temperature at 144 K where we see doubling of lattice parameter c [4].

With evidence from neutron scattering, it has been shown by Mir *et.al* [4] that there is a structural transition at 283K. This structural transition is due to displacement of the metal ion in the central rung which leads doubling of the lattice parameter c, as indicated in figure 1.4. As we can see that the central 3+ ion shifts to one of the either side of the rung. Displacement of central metal ions leads to a charge ordering in the rung of three leg ladder [5] which was experimentally observed in Larra *et.al* [6] using Mössbauer spectroscopy.

Below 112 K, Fe^{3+} ions along the rung of ladder orders antiferromagnetically and below 40 K rest of the ions order ferromagnetically leading to a weak ferromagnetism in $Fe_3O_2BO_3$. The magnetic structure at 82 K and 10 K are shown in the figure 1.5. This ordering of magnetic moments in ladder at 112K proves that the interaction in triads is much larger than that of other magnetic ions. In each rung, the coupling is ferromagnetic but along the c direction coupling is antiferromagnetic in nature as shown in figure 1.5a. Below 70 K rest of the magnetic ions starts to order ferromagnetically. The magnetic structure below 40K is still debatable. Some observe weak ferromagnetic behavior while there are some reports, where ferromagnetism disappears [5].

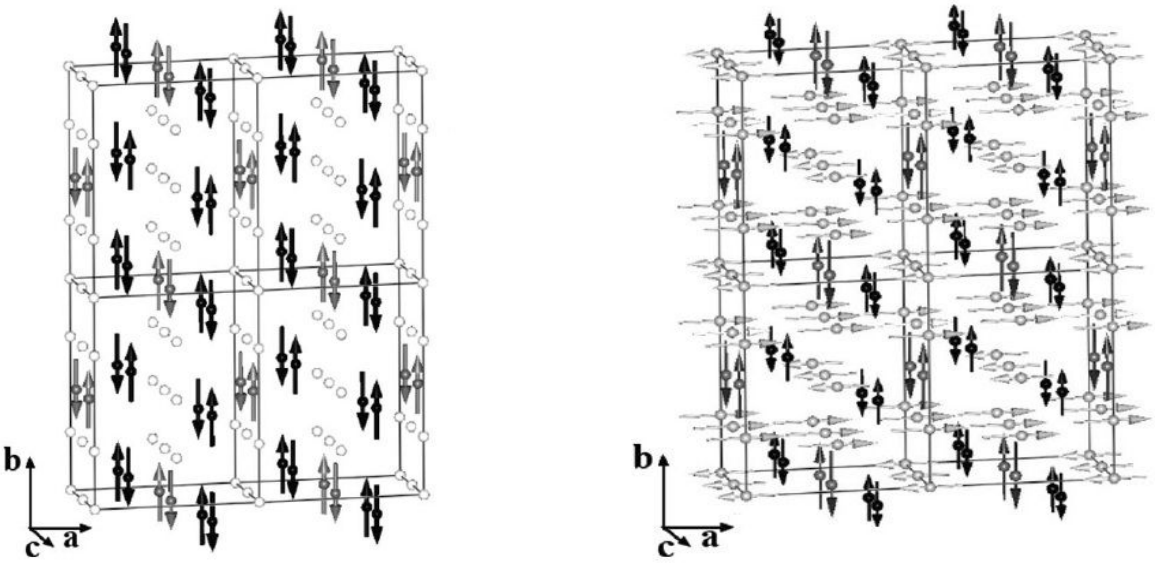

(a) (b)

Figure 1.5: Magnetic structure of $Fe_3O_2BO_3$ (a) At 82 K: Fe1 & Fe3: white (no magnetic ordering); Fe2: gray, Fe4a, Fe4b: black (Antiferromagnetic), (b) At 10 K: Fe1 & Fe3: light gray (Ferromagnetic); Fe2: dark gray, Fe4a, Fe4b: black (Antiferromagnetic) [5]

1.1.3 A Hetrometallic ludwigite: $Co_{2.4}Ga_{0.6}O_2BO_3$

$Co_{2.4}Ga_{0.6}O_2BO_3$ has Co^{3+} ions as well as Co^{2+} ions present with Ga^{3+} ions, and the structure is given in figure 1.6. There are four cobalt atoms present for every gallium ion in this ludwigite.

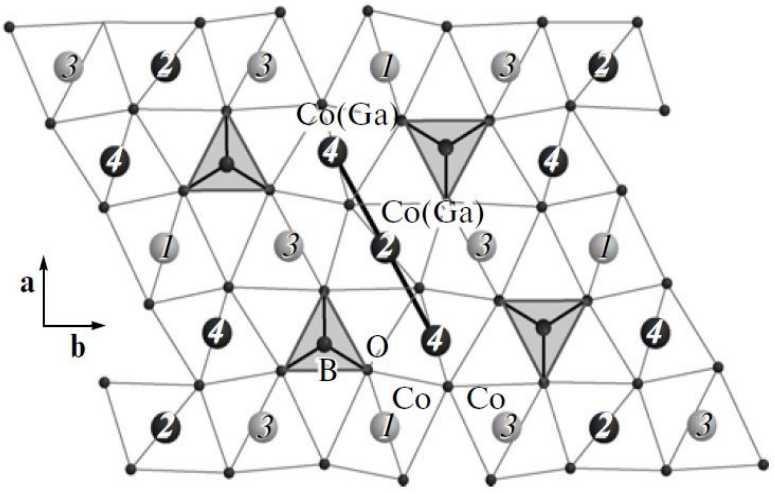

Figure 1.6: Crystal structure of $Co_{2.4}Ga_{0.6}O_2BO_3$ projected along the c direction with different metal ion positions numbered. The shaded triangles are orthoborate group BO_3 [3]

Calculating the electric feild gradient experienced by metal ion positions using equation 1.1 given in [3].

$$V_{zz} = \sum 2e \frac{3(\cos^2 \beta) - 1}{r^3} \tag{1.1}$$

Where V_{zz} is the electric field along the principal axis of oxygen octahedra. β is the angle between principal axis and direction toward neighboring oxygen ion and r is the distance with metal ion and oxygen. As reported in [3] metal ion site 4 has the lowest electric field gradient, thus it is preferable for a symmetric metal ion. Also site 4 is in the middle of a zig-zag wall (see figure 1.6) and has the smallest isotropic displacement parameter. Thus a symmetric 3+ ion prefers the metal ion position 4 in ludwigites. These ions are less occupied in metal ion site 2 and rarely occupy site 3 and 1 [3].

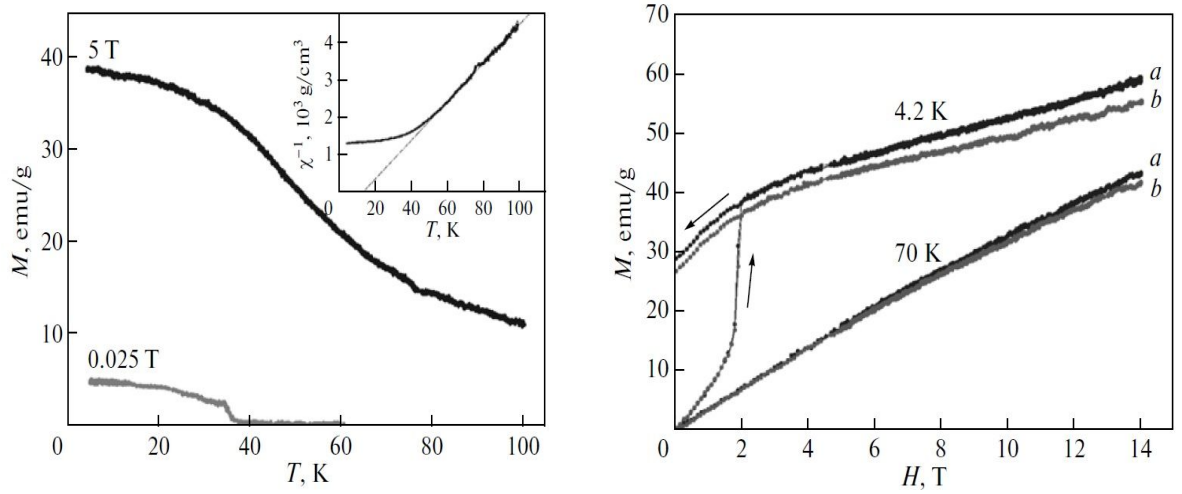

(a) (b)

Figure 1.7: (a) ZFC and FC magnetic measurement of $Co_{2.4}Ga_{0.6}O_2BO_3$ shows transition around 37 K (Inset: χ^{-1} shows linear behavior above transition temperature), (b) Magnetization(M) versus Field(H) measurements of $Co_{2.4}Ga_{0.6}O_2BO_3$ along a & b axis which shows metamagnetic transition around 2T at 4 K and shows paramagnetic behavior at 70 K [3].

Bulk magnetic measurements of $Co_{2.4}Ga_{0.6}O_2BO_3$ shows a magnetic transition at 37 K [3]. Figure 1.7a shows the zero feild cooled (ZFC) and field cooled (FC) measurements along the crystallographic a direction at a field of 250 Oe. For FC measurement the sample was cooled at 5T. The inset in figure 1.7a shows susceptibility inverse versus temperature. Magnetization versus Field plot of $Co_{2.4}Ga_{0.6}O_2BO_3$ along crystallographic a and b direction is reported, which shows a metamagnetic transition as shown in figure 1.7b. At 4.2K we can see a metamagnetic transition along both a and b directions around 2T. At 70K the material is purely paramagnetic in nature.

The above comparison of the magnetic properties of two different ludwigites shows that the magnetic properties of a ludwigite is highly dependent on the type of metal ions present and the crystallographic position where these metal ions resides. An extensive list of magnetic transition temperature of ludwigites are given in table A.1, appendix A.

1.1.4 Why Ludwigites are interesting?

The origin of multiferroicity in some materials have been traced back to its charge ordering [7], weak ferromagnetic behavior [8] [9] [10] or structural transitions [11]. As mentioned above that some of the homometallic ludwigites show charge ordering along with a structural transition. Similarly most of the ludwigites, both homometallic and hetrometallic show weak ferromagnetism at low temperature. Thus pointing towards the fact that these class of materials might be multiferroic or magnetoelectric in nature. Since most of the ludwigites have been widely studied because of its three leg ladder (triads) and weak ferromagnetism, we aimed to study the properties of less explored ludwigites.

Multiferroic materials have a characteristic ferroelectric transition, which is typically observed in dielectric constant measurements. Other than the ferrelectric transition, dielectric constant measurements also show magnetodielectric effect. When dielectric constant of a material is coupled to magnetization we can see magnetodielectric effect. This can be seen as a change in dielectric constant under the application of magnetic field [12] [13]. Since we are not studying the properties of homometallic ludwigites it is highly probable that the transitions observed in dielectric measurements are not ferroelectric but rather magnetodielectric.

1.2 Magnetodielectric effect

Magnetodielectric effect is seen when dielectric constant is coupled to the magnetic properties of the material. $SeCuO_3$, $TeCuO_3$, and $Ni_3V_2O_8$ are some of the well known materials which show magnetodielectric effect [13]. Due to symmetry restrictions only very few magnetic point groups allows the coexistence of magnetization, polarization and magnetodielectric effect [14].

1.2.1 Basic theory of Magnetodielectric effect

Consider a simple expansion of Landau free energy in terms of electric polarization (P), magnetization (M) [13].

$$F = \frac{1}{2\epsilon_o}P^2 - P \cdot E - \alpha PM + \beta PM^2 + \gamma P^2M^2 + \cdots \tag{1.2}$$

In the equation 1.2, α, β and γ are coupling constants between electric polarization and magnetization and E is electric field. Because of symmetry reasons, in most

materials, the third term is forbidden [13]. Dielectric constant of a material is related to second derivative of the free energy expansion with respect to polarization. So the first term that contributes to the correction of dielectric constant in a material is $\gamma P^2 M^2$. Hence dielectric constant is ϵ_o with an added correction proportional to γM^2 in magnetodielectric ferromagnets.

In case of antiferromagnets the above explanation will not work because there is no bulk magnetization in the system. The change in dielectric constant is thus dependent on the correlation between magnetization at different locations [15]. For a given wave vector q let M_q be the magnetization. Then for antiferromagnets, the corrected free energy will be given by equation 1.3 [15].

$$F = \frac{1}{2\epsilon_o} P^2 - P \cdot E + P^2 \sum_q g(q) < M_q M_{-q} > (T) + \cdots \tag{1.3}$$

In the equation $g(q)$ is a function of wave vector q. $< M_q M_{-q} > (T)$ is the q dependent correlation between magnetization at M_q and M_{-q} at a given temperature T. The actual value of polarization is thus given as [13]

$$P = \frac{E}{\frac{1}{\epsilon_o} + 2\sum_q g(q) < M_q M_{-q} > (T)} \equiv \epsilon E \tag{1.4}$$

Where ϵ is defined as

$$\epsilon = \frac{\epsilon_o}{1 + 2\epsilon_o \sum_q g(q) < M_q M_{-q} > (T)} \tag{1.5}$$

Equation 1.5 gives the dielectric constant for a given magnetodielectric material. Where ϵ_o is the bare dielectric constant and the rest is shift in dielectric constant due to magnetodielectric effect.

The equations 1.4 and 1.5 only gives a set of formal understanding of magnetodielectric effect, based on spin-phonon interaction in a material. In normal materials the small displacement of atoms is very weakly coupled ($\sim$ not coupled) to magnetic order. Thus magnetic ordering is insensitive to slight atomic displacements by thermal noise. But in materials with strong spin-lattice coupling, ordering of spins leads to change in dielectric constant because of the change in optical phonon frequencies [13]. So the function g(q) physically represents the coupling of phonons and magnetic order. It is proposed by Lawanti *et.al* [15] that the functional form of g(q) can be obtained from the expansion of magnetic exchange integral with respect to atomic displacements.

$$g(q) = \gamma(1 - \cos(qR)) \tag{1.6}$$

Thus the approximate from of g(q) is given in equation 1.6 which is only valid for long wavelength q modes. Where R is the displacements between nearest neighbors. γ is

the coupling constant which is dependent on the second derivative of exchange integral, square of mean lattice position and correlation of spins at wave vector q and -q [15]. The value of g is maximum when the wave vector is close to the Brillouin zone boundary.

From equation 1.5, the paramagnetic region, there is a fixed correlation between spins which will be showed as a slight shift in dielectric constant. In the ferromagnetic phase, this correlation goes to zero thus implying that there would be a small jump in ϵ around T_c. The case of antiferromagnetic materials exhibiting magnetodielectric effect is best explained by the figure 1.8 which shows g(q) has its maximum value towards the zone boundary. So if g(q) and $< M_q M_{-q} >$ coincide, which is the case in antiferromagnetic systems, large magnetodielectric effect is observed, while if they do not coincide the magnetodielectric effect goes to zero.

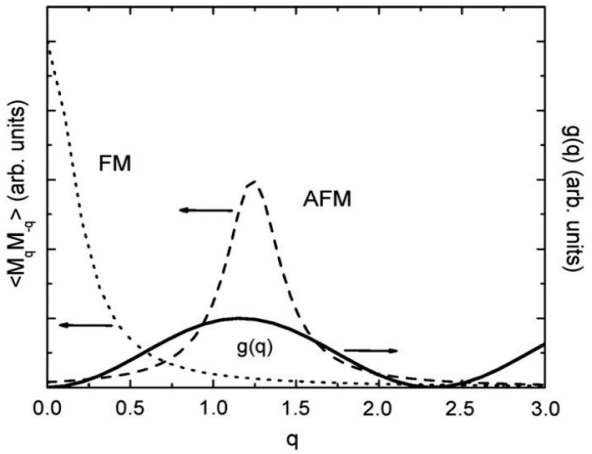

Figure 1.8: Solid line represents g(q) and the dotted lines shows the correlation of spins ($< M_q M_{-q} >$) in ferromagnetic and antiferromagnetic order [13].

1.2.2 Examples of Magnetodielectric effect

$SeCuO_3$ and $TeCuO_3$ are ferromagnetic and antiferromagnetic materials and magnetodielectric effect in these materials can be explained using the above physical picture. The temperature dependence of dielectric constant at different magnetic fields are shown in the figure 1.9

It has been shown in [15] that the dielectric constant of $SeCuO_3$ is proportional to M^2 thus giving support to equation 1.2. In antiferromagnetic $TeCuO_3$, application of very high magnetic fields leads to suppression of antiferromagnetic correlations and thus reduces the dielectric constant. Both of these effects can be seen in figure 1.9.

In case of $Ni_3V_2O_8$ there is ferroelectric transition around 6.3K. Below 3.2K $Ni_3V_2O_8$ shows a canted antiferromagnetic phase with small ferromagnetic moment in (001) direction [13]. The temperature dependence of dielectric constant is given in the figure 1.10a which shows ferroelectric transition and change in dielectric constant dur-

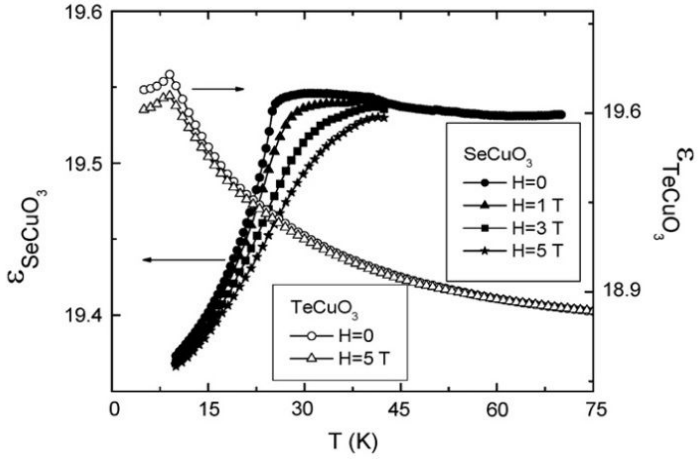

Figure 1.9: Temperature variation of dielectric constant of $TeCuO_3$ and $SeCuO_3$ at different magnetic fields. In both ferromagnetic $SeCuO_3$ and antiferromagnetic $TeCuO_3$ the dielectric constant reduces as feild increases [13].

ing the transition to canted antiferromagnetic order. Figure 1.10b shows the shift in transition temperature as a magnetic field is applied along (001) direction of the canted antiferromagetic low temperature phase of $Ni_3V_2O_8$.

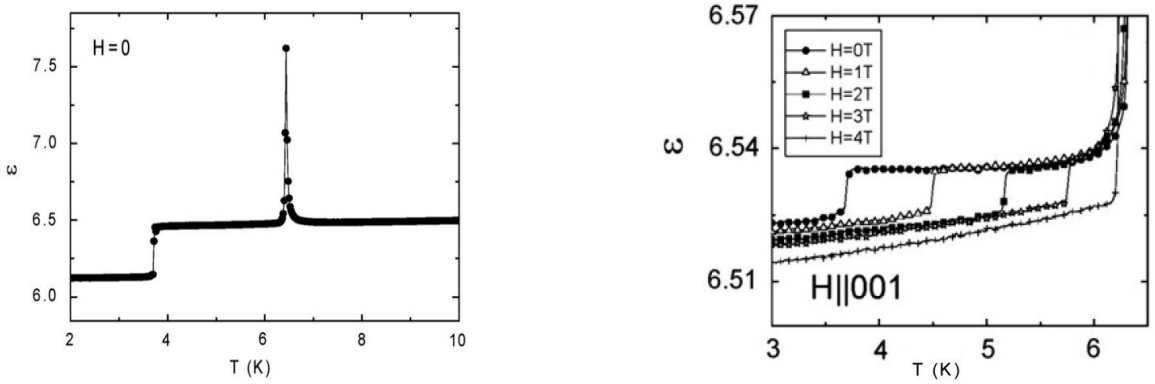

(a) (b)

Figure 1.10: Temperature dependence of dielectric constant in $Ni_3V_2O_8$, (a) At zero magnetic field. (b) At different magnetic field applied along the (001) axis, Transition temperature shifts with increasing magnetic field [13].

1.3 Magnetocaloric Effect (MCE)

Magnetocaloric effect (MCE) essentially means the heating or cooling of a magnetic material by varying the applied magnetic field [16]. Phase transitions are related the to a change in entropy of the system. Thus, under isothermal conditions there will be a change

in entropy across the transition temperature. In Ludwigite systems there is probability of a structural transition combined with a magnetic transition. In such cases, the MCE (entropy change) will be huge which will be detectable in specific heat measurements at different magnetic fields. So it is important to discuss the basics of MCE and how it is being calculated.

This phenomena can be explained very easily if we use magnetic field and magnetization as classical thermodynamic variables. Consider the case of a ferromagnet, where the entropy of the system can be divided into three major components, first being from lattice contribution, second is electronic and third is dependent on the magnetic field experienced by the material [16].

$$S(T,H) = S_{lattice}(T) + S_{electronic}(T) + S_M(T,H) \tag{1.7}$$

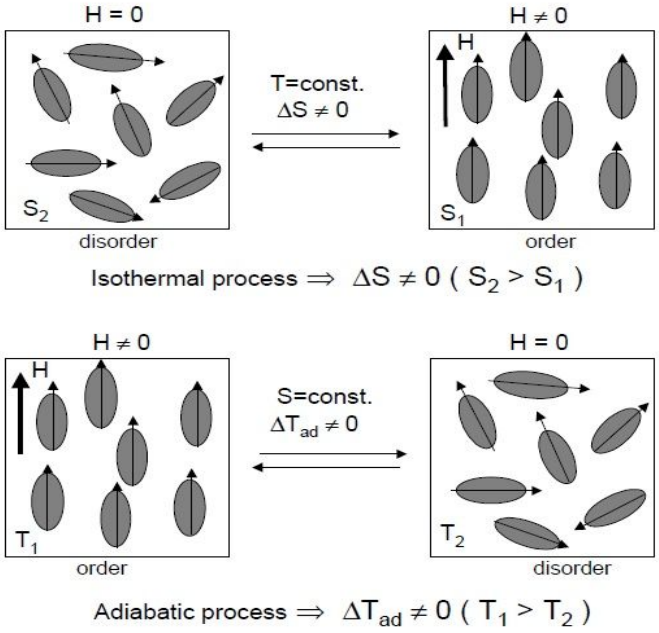

Figure 1.11: Diagram showing MCE in Isothermal (Change in entropy) and Adiabatic conditions (Change in temperature) [12].

The figure 1.11 shows a schematic representation of how application of magnetic field reduces the entropy (or temperature) in an isothermal (or adiabatic process). Both of the above processes are reversible in nature. Let ΔS_M be the entropy change in an isothermal process where S_M and S_O represents the total entropy at magnetic field $(H \neq 0)$ and $(H = 0)$. Considering Maxwell's equation in thermodynamics.

$$\left(\frac{\partial S(T,H)}{\partial H}\right)_T = \left(\frac{\partial M(T,H)}{\partial T}\right)_H \tag{1.8}$$

Integrating the above equation 1.8 considering a constant temperature and volume process we get

$$\Delta S_M(T, \Delta H) = \int_{H=0}^{H\neq 0} \left(\frac{\partial M(T,H)}{\partial T}\right)_H dH \tag{1.9}$$

It is important to note that,

1. Temperature Increases $\implies$ Magnetization decreases $\implies$ $\left(\frac{\partial M(T,H)}{\partial T}\right)_H < 0$
   So entropy change is negative provided $\Delta H > 0$.

2. $\left|\left(\frac{\partial M(T,H)}{\partial T}\right)_H\right|$ is maximum at transition temperature $\implies$ $|\Delta S_M(T, \Delta H)|$ is maximum at the same temperature.

1.3.1 Measurement of MCE

In an adiabatic cycle, let T_o and T_f be the initial and final temperature of sample after a change of magnetic feild ΔH. This temperature change gives a direct way of measuring MCE.

$$\Delta T_{ad}(T_o, \Delta H) = T_f - T_o \tag{1.10}$$

There are indirect ways of measuring MCE. Measuring heat capacity at different magnetic fields gives change in entropy of a system.

$$S(T)_{H\neq 0} = S(T)_{H=0} + \int_0^T \frac{C(T)_{P,H}}{T} dT \tag{1.11}$$

Measuring heat capacity and integrating $\frac{C(T)_{P,H}}{T}$ with respect to temperature gives entropy change in a given solid. It is worth noting that the error in $\Delta S_M(T, \Delta H)$ is strongly dependent on the accuracy of measurement of heat capacity $C(T)_{P,H}$ and method used for integration.

The above figure 1.12 shows the calculated change in entropy for Gd from specific heat measurement at 0T to 5T. As mentioned earlier the entropy change is negative for a given positive magnetic field. Maximum entropy change is observed in the vicinity of the transition temperature.

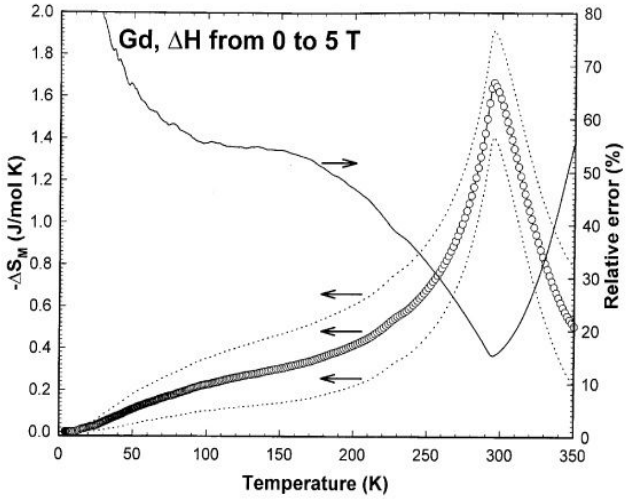

Figure 1.12: MCE in Gd for a magnetic field of 5T (open circles), Relative error (solid line), Range of absolute error (dotted lines)[12]

1.4 Paramagnetism and Crystal field splitting

It is important to understand the basics of quantum theory of paramagnetism to analyze the magnetic measurements of ludwigites at high temperatures. All the metal ions in ludwigites are present in oxygen octahedra, thus the outer d orbitals of metal ions will experience an inhomogeneous external electric field (crystal field). This leads to crystal feild splitting in the d orbitals. This effect also has to be taken into account while analyzing paramagnetism in ludwigites.

1.4.1 Paramagnetism

The magnetic moment $\boldsymbol{\mu}$ of an atom or ion is given by total angular momentum $\mathbf{J}$ as given by equation 1.12 where g is Landae g factor given by equation 1.13. J, L and S are quantum numbers of angular momentum, orbital angular momentum and spin angular momentum respectively.

$$\boldsymbol{\mu} = -g\mu_B \mathbf{J} \tag{1.12}$$

$$g = 1 + \frac{J(J+1) + S(S+1) - L(L+1)}{2J(J+1)} \tag{1.13}$$

Using quantum statistical mechanics, considering an applied magnetic field of H, total magnetization of a collection of N atoms or ions is given by equation 1.14 [17] where B_J is Brillouin function which is given by $B_J(x)$

$$M = NgJ\mu_B B_J(x) \tag{1.14}$$

$$B_J\left(x = \frac{gJ\mu_B H}{k_B T}\right) = \frac{2J+1}{2J}\coth\left(\frac{(2J+1)x}{2J}\right) - \frac{1}{2J}\coth\left(\frac{x}{2J}\right) \tag{1.15}$$

k_B and T are Boltzmann constant and temperature. In paramagnetic region where factor $x \ll 1$, the above magnetization can be reduced to the form given by 1.16 and μ_{eff} known as effective Bohr magneton is given by 1.17. C is curie constant.

$$\chi = \frac{M}{H} = \frac{N(\mu_B \mu_{eff})^2}{3k_B T} = \frac{C}{T} \tag{1.16}$$

$$\mu_{eff} = g\sqrt{J(J+1)} \tag{1.17}$$

Effective magnetic moment of a spin only system can be calculated from formula 1.18. The same equation is used for calculation of effective magnetic moment of transition metal ions in table 1.1.

$$\mu_{eff} = 2\sqrt{S(S+1)} \tag{1.18}$$

1.4.2 Crystal Field Splitting

When a transition metal ion is placed in a highly inhomogeneous electric feild, the outer orbitals split into different energy levels depending on the symmetry of the electric feild which is known an crystal feild splitting [17]. This usually happens in metal oxides where d orbitals of the transition metal are covalently bonded with oxygen p orbitals. When the ion is placed in an octahedrally symmetric environment, the outermost d orbitals are split into two energy levels (t_{2g} and e_g). The ones in axial direction are of higher energy while the d orbitals in off axis are of lower energy. The exact opposite happens when there is a tetrahedral coordination with oxygen and metal ion. When the pairing energy is higher than the energy difference between the t_{2g} and e_g levels, we observe a high spin state. If the splitting energy is much higher than the pairing energy we observe low spin state. Representation of high spin state partially filled d orbitals are shown below.

Tetrahedral symmetry

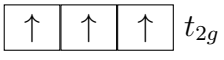

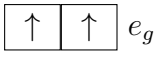

Octahedral symmetry

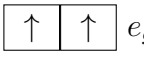

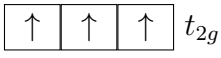

When a inhomogeneous electric field is applied, orbital angular momentum is no longer constant and will give net average of zero. Thus, the contribution from orbital

angular momentum to the magnetism of ion or atom will average out to zero. This is called quenching of orbital angular momentum. In most cases, spin part only contributes to the magnetism of transition metal ions/atoms in a crystal field.

The calculated magnetic moments of transition metal ions in octahedral symmetric environment which are being used in this project is shown below.

Table 1.1: Magnetic moment of Co^{2+}, Co^{3+} and Ni^{2+} in high and low spin configurations.

Ion	General Electronic configuration	Low spin state Electronic configuration	Magnetic Moment low spin state μ_B	High spin state Electronic configuration	Magnetic Moment High spin state μ_B
Co^{2+}	[Ar] $3d^7$	$\uparrow$ $\square$ e_g $\uparrow\downarrow$ $\uparrow\downarrow$ $\uparrow\downarrow$ t_{2g}	1.7321	$\uparrow$ $\uparrow$ e_g $\uparrow\downarrow$ $\uparrow\downarrow$ $\uparrow$ t_{2g}	3.8730
Co^{3+}	[Ar] $3d^6$	$\square$ $\square$ e_g $\uparrow\downarrow$ $\uparrow\downarrow$ $\uparrow\downarrow$ t_{2g}	0	$\uparrow$ $\uparrow$ e_g $\uparrow\downarrow$ $\uparrow$ $\uparrow$ t_{2g}	4.8990
Ni^{2+}	[Ar] $3d^8$	$\uparrow$ $\uparrow$ e_g $\uparrow\downarrow$ $\uparrow\downarrow$ $\uparrow\downarrow$ t_{2g}	2.8284	$\uparrow$ $\uparrow$ e_g $\uparrow\downarrow$ $\uparrow\downarrow$ $\uparrow\downarrow$ t_{2g}	2.8284

1.5 Plan of the Project

The starting aim of this project was to identify if there are any multiferroicity in Ludwigites. We decided to synthesize alumino-ludwigites which are very less studied. This new ludwigites we synthesized using flux growth. We used Rietveld refinement to confirm the crystal structure from X-ray diffraction data obtained at room temperature. After successful sample synthesis, bulk magnetic and dielectric measurements were done which could give clues to the possible magnetodielectric and magnetocaloric behavior of ludwigites. According to the results observed, further physical investigations are currently being carried out on these alumino-ludwigite samples.

Chapter 2

Experimental Techniques

2.1 Sample synthesis

Borates are usually grown by flux growth. Flux growth is basically growth of crystals in a solvent (flux). The stoichiometric amount of reactants are mixed with a flux or a mixture of fluxes and the reaction is carried out at a much higher temperature than the melting point of the flux. Then reaction mixture is slowly cooled till the melting point of the flux. After the reaction flux is either removed physically or by some solvents which will dissolve the flux keeping the sample intact. The most common type of flux used is nonreactive flux, which only aids the reaction and in formation of crystals. While reactive flux not only aids the formation of crystals but also takes part in reaction as a reactant.

Flux used in the synthesis of ludwigites is either borax ($Na_2B_4O_7 \cdot 10H_2O$) or boric acid (H_3BO_3) or a mixture of both. Also both fluxes are reactive fluxes and highly reactive towards alumina at high temperatures. So the only possible ludwigites that can be synthesized using alumina crucibles are alumino-ludwigites.

2.1.1 Synthesis of $Ni_2AlO_2BO_3$ and $Co_2AlO_2BO_3$

Both of these ludwigites have been synthesized in the past and its structure has been reported in Hriljac *et.al* [18] and K. Bluhm *et.al* [19]. The first one uses only borax as a flux, with no aluminum oxide added and the reaction was carried out at 1000^oC in alumina crucible. In the latter, a mixture of borax and B_2O_3 is used as flux and the reaction was carried out at 1300^oC. Trying synthesis in both routes did not yield a single phase of the compounds expected. We created a new method in which pure state of both the samples can be obtained using flux growth.

Stoichiometric amount of the metal oxides (including Al_2O_3) were taken and then mixed with excess borax ($Na_2B_4O_7 \cdot 10H_2O$) (5 times the amount of transition metal oxide), ground well using ball mill at 120 rpm for 12 hours to make a fine homogeneous mixture. This reaction mixture was then transfered to a big alumina crucible and was fired at 1000^oC. For $Ni_2AlO_2BO_3$, reaction was carried out for 12 hours at 1000^oC and then cooled till 740^oC at the rate of 5^oC per hour. At 740^oC the furnace was turned off

for fast cooling, since borax solidifies at 750^{o}C. $Co_2AlO_2BO_3$ was synthesized in the same reaction procedure as mentioned above, but the reaction time at 1000^{o}C was increased to 90 hours. The reaction conditions are summarized below.

Table 2.1: Summarizing reaction conditions of $Ni_2AlO_2BO_3$ and $Co_2AlO_2BO_3$

Sample to be prepared	Reactants required	Reaction time at 1000^{o}C	Cooling rate till 740^{o}C
$Ni_2AlO_2BO_3$	NiO, Al_2O_3 and excess Borax	12 hours	5 ^{o}C/hour
$Co_2AlO_2BO_3$	Co_3O_4, Al_2O_3 and excess Borax	90 hours	5 ^{o}C/hour

After the reaction, crucible was broken and sample was extracted out from it. In the case of $Ni_2AlO_2BO_3$ there was a patch of green NiO present in the middle of the crucible which was physically separated from the sample. The figure 2.1 shows pictures of both samples after the reaction. To remove excess flux after the reaction, the samples were washed with warm dilute hydrochloric acid for four days with changing the solution once in two days. This was then washed again with distilled water to make sure that there were no traces of any borates. Unfortunately powder X-ray diffraction (XRD) showed a slight impurity of NiO in $Ni_2AlO_2BO_3$. The above reaction technique gives a yield of approximately 40% for both the ludwigites.

(a) (b)

Figure 2.1: Photos of sample after reaction (a) $Co_2AlO_2BO_3$ after reaction (blue color sample stick to the walls are cobalt oxides which was washed out by HCl) (b) $Ni_2AlO_2BO_3$ after reaction (green patch in center is nickel oxide)

We have tried synthesizing other compounds like $Ni_2FeO_2BO_3$ and $Fe_3O_2BO_3$ using alumina and platinum crucibles but our trials did not yield a single phase. A summary of these reactions can be seen in appendix B.

2.2 X-ray Diffraction (XRD)

X-ray diffraction of the powder samples were done using powder X-ray diffraction facility of Bruker D8 Advance Powder X-ray Diffractometer at IISER Pune. This facility uses Cu K_α radiation with $\lambda = 0.15406$ nm. XRD of powder samples were done at room temperature where X-ray source and detector which are rotated by 2θ and the sample orientation is fixed. The well ground sample is mounted on a glass slide, with the assumption that all crystallographic planes are exposed to X-ray beam. The intensity of Bragg scattered X-rays were recorded electronically, and the output was given as 2θ versus intensity (arbitrary units). Peaks in the output graph corresponds to crystallographic planes given by (hkl) values. For preliminary conformation of the phase, International Centre for Diffraction Data (ICSD) database was used to compare the XRD pattern with previously reported diffraction patterns.

2.3 Structural analysis

The most well accepted method for analysis of powder XRD is by Rietveld refinement. This technique was first proposed and developed by Hugo M. Rietveld in 1969 [20] which uses least square refinement.

2.3.1 Mathematical Model of Rietveld refinement

Rietveld refinement is strongly dependent on the quantity which is being minimized in each iteration of the program which is given by equation 2.1 [21].

$$S_y = \sum_{y_i} w_i (y_i - y_{ci})^2 \tag{2.1}$$

where sum is over all i^{th} step and the parameters are

S_y = Residual quantity which is refined,
y_i = Intensity observed in i^{th} step,
y_ci = Intensity calculated in i^{th} step,
$w_\mathrm{i} = 1/\mathrm{y_i}$

Intensity calculated I_K for a Bragg peak K given by Miller indices (hkl) is dependent on the square of the absolute value of structure factor F_K. The structure factor is defined by the equation 2.2 [21].

$$F_K = \sum_j N_j f_j \exp[2\pi i(hx_j + ky_j + lz_j)] \exp[-8\pi^2 u_{js}^2 \sin^2\theta/\lambda] \tag{2.2}$$

where u_{js} is defined as root mean square thermal displacement of j^{th} atom in direction s parallel to the diffraction vector[21]

h, k, l = Miller indices,
x_j, y_j, z_j = Position of j^{th} atom in a unit cell,
N_j = Occupancy multiplier of j^{th} atom,
f_j = Atomic form factor of j^{th} atom

For a given powder diffraction pattern of a crystalline material, Bragg intensity at a specific step i will be dependent on all the intensity contributions from a specified angle in addition to the background intensity. y_{ci} is calculated based on [21].

$$y_{ci} = s \sum_K L_K |F_k|^2 \phi(2\theta_i - 2\theta_K) P_K A + y_{bi} \tag{2.3}$$

Parameters in the above equation are defined as

s = Scale factor,
K = Miller indices (hkl) for given a Bragg peak,
L_K = Lorentz polarization and multiplicity factors,
ϕ = Bragg reflection profile function (details are given in [21], chapter 1, table 1.2),
P_K = Preferred orientation function,
A = Absorption factor,
F_K = Structure factor,
y_{bi} = Background intensity at i^{th} step.

Bragg reflection profile function ϕ gives each peak a shape which is calculated including instrumental corrections, asymmetry, sample displacement, transparency and size shape and strain effects. The full width half maximum (FWHM) (H) of a Bragg peak function is defined in equation 2.4 where U, V and W are parameters refined in the program.

$$H = \sqrt{U \tan^2\theta + V \tan\theta + W} \tag{2.4}$$

2.3.2 Criteria for fit

The criteria to fit a given pattern depends upon the R values that are being used in Rietveld refinement. R values helps to determine that if the fit has reached a global minimum and also it gives goodness of the fit. The complete set of R values can be seen in [21] Chapter 1 table 1.3. The most important of the R value is R-weighted pattern (R_{wp}) given in equation 2.5 [21].

$$R_{wp} = \left[\frac{\sum w_i (y_i(obs) - y_i(cal))^2}{\sum w_i (y_i(obs))^2} \right]^{\frac{1}{2}} \tag{2.5}$$

To define the goodness of a fit we need to define the next important R value which is R-expected (R_e) given by equation 2.6 where N represents number of observations made and P represents number of parameters refined in a given cycle. Goodness of a given peak is the ratio of R-weighted pattern to R-expected equation 2.7 [21].

$$R_e = \left[\frac{N-P}{\sum w_i(y_i(obs))^2}\right]^{\frac{1}{2}} \tag{2.6}$$

$$S = \frac{R_{wp}}{R_e} \tag{2.7}$$

For a given fitting to be called good, the goodness of fit must be close to 1. It is adequate to have a fit with goodness 1.3 [21]. If a fit gives goodness much greater or less than 1 then the fit is probably wrong. Rietveld refinement provides a way to extract a large amount of information from a single X-ray diffraction pattern and thus is the most important tool to analyze an XRD pattern. This refinement method can also be used to solve magnetic structures of a given material using neutron diffraction data.

Some of the common softwares that uses Rietveld refinement method are FullProf Suite and GSAS. We have used FullProf Suite [22] software to fit our powder XRD patterns.

2.4 SQUID Magnetometer

Bulk magnetic measurements were done on samples using a SQUID (Superconducting Quantum Interference Device) designed by Quantum Design (MPMS/XL). The SQUID magnetometer [23] works on the principle that when a magnetic material is passed through a Josephson junction [24] superconducting ring, a voltage imbalance is created. Current induced in the superconducting ring exceeds the critical current of a Josephson junction thus producing a voltage which is detectable and gives a direct method to measure magnetization of a sample [25]. SQUID is the most sensitive device to measure the bulk magnetization of a given system.

Figure 2.2 shows basic setup of detection coils in a SQUID magnetometer. There are four detection coils in which top and bottom ones are wound anticlockwise and two detection coils in the center are wound clockwise. This setup ensures that the noise in the measurement is less by producing opposite direction currents for local variation of the magnetic field. These local changes are expected when the magnetization induced by the sample is non uniform across the four detection coils [26].

The main two techniques used for magnetic measurement is SQUID are D.C. technique and Reciprocating sample option (RSO) technique [26]. In DC technique sample is moved through the detection coils in one point at a time and magnetization is recorded

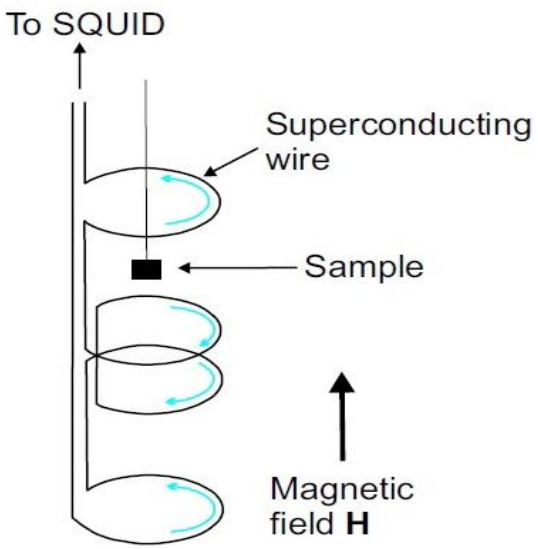

Figure 2.2: SQUID detection coils [26]

as at each position. In RSO technique, the sample is oscillated along the central coils and magnetization is measured a function of sample position [26]. RSO technique is more sensitive but it has a cut-off at 5 e.m.u. in Quantum Design MPMS/XL. Thus for most of the magnetization measurements of our samples the DC transport option was used.

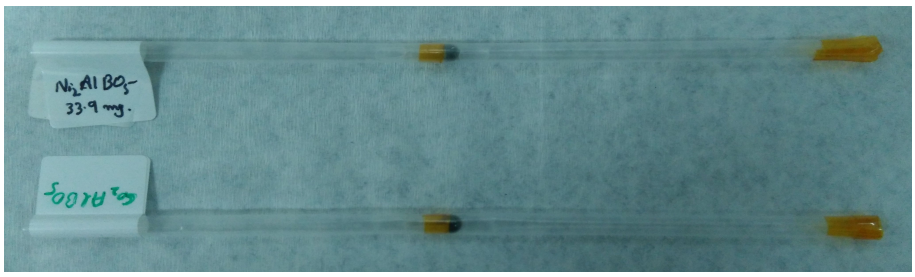

Figure 2.3: Sample holder with plastic straw and capsule filled with powdered sample

For magnetization measurements, well ground sample was first placed in a gelatin capsule and sealed with kapton tape. This capsule is then inserted to a plastic straw and the bottom of the straw was sealed with kapton tape. This was then attached to sample holder and then inserted into magnetometer. The figure 2.3 shows sample prepared to be attached to sample holder. At first, the sample is centered at room temperature. For Zero field cooled (ZFC) measurement, sample is first cooled in zero field and magnetization is measured in a positive magnetic field of 100 Oe within specific intervals of temperature while system is being heated up. For Field cooled (FC) measurements the same procedure of measurement is done except the sample is cooled in a nonzero magnetic field. Magnetization versus field measurement was done in an applied fields from -7 T to +7 T.

2.5 Dielectric Measurement

The dielectric constant of a material can be calculated the from capacitance of a parallel plate geometry, with the dielectric material in between the plates. For dielectric measurements of my sample, first pellets of powder sample was made using a KBr pelletizer with diameter approximately 13mm and thickness slightly above 1.2mm. A dense pellet is required for the dielectric measurement of a polycrystalline sample, thus reducing the error in dielectric constant due to air captured inside the vacant spaces in the sample. To make a dense pellet, during the process of pellet making a binder PVA (Polyvinyl alcohol) solution was mixed with the sample. This acts as a glue, and holds the micron sized particles together, increasing density of the sample. The pellets were sintered at 850^{o}C for the binder to evaporate, thus giving a strong, dense pellet. Silver paste is applied on both faces of the pellet to ensure good electrical contact. This pellet was then inserted between two parallel plate electrodes, and the impedance was measured at different frequencies and temperatures, using a four probe measurement technique. This impedance was then deconvoluted into real and imaginary parts of the complex dielectric constant.

$$\epsilon_{\mathbf{r}} = \epsilon_r'(\omega) + i\epsilon_r''(\omega) = |\epsilon_{\mathbf{r}}| \exp^{i\delta} \tag{2.8}$$

where

$\epsilon_{\mathbf{r}}$ = Complex dielectric constant
ϵ_r' = Real part of dielectric constant,
ϵ_r'' = Imaginary part of dielectric constant,
δ = Loss angle (ratio of ϵ_r'' to ϵ_r')

In equation 2.8 the real part represents the energy stored in medium while the imaginary part gives energy loss in a given medium.

For temperature variation, a closed cycle refrigerator (CCR) designed by Cryo industries, was used with a Lakeshore temperature controller (model 335), and temperature was varied from 15 K to 300 K. The measurement was usually done when the system is being warmed. The frequency analyzer used for the measurements was Novocontrol Alpha-A High Performance Modular Measurement System, which has operating frequency range of 30μHz to 4$\times 10^7$ Hz and impedance range from -0.001 to 10^{15} Ω. Our dielectric measurements were carried out in the range of 100Hz to 30MHz.

2.6 Heat capacity measurement

The heat capacity measurement was done using Physical property measurement system (PPMS) Quantum Design (Evercool-II). Some magnetic field dependent measurements were also done at TIFR using a liquid helium PPMS. For heat capacity measurement a small piece of pelletized sample was used. First a thin layer of Apiezon N grease is used

to give good thermal contact of sample to the platform where heater and thermometer is attached [27].

The heat capacity of the Apiezon N grease was measured first and then total heat capacity of Apiezon N grease and sample is measured. The heat capacity of sample is thus the difference in heat capacity of first two measurements. The sample size used was around 3-4mm $\times$ 3-4mm with a average mass of 10 mg. To prevent heat loss due to convection high vacuum is a prerequisite. Heat capacity of $Co_2AlO_2BO_3$ and $Ni_2AlO_2BO_3$ was measured at different magnetic fields around their transition temperatures.

Chapter 3

Results and Discussion

In this chapter, the data which we have obtained on $Ni_2AlO_2BO_3$ and $Co_2AlO_2BO_3$ are reported and analyzed.

3.1 $Ni_2AlO_2BO_3$

3.1.1 Structural analysis of $Ni_2AlO_2BO_3$

The structure of $Ni_2AlO_2BO_3$ was analyzed using Rietveld refinement of powder XRD pattern of the sample. During the Rietveld refinement of $Ni_2AlO_2BO_3$, it was found out that there was a small impurity peak which belonged to the (200) peak of NiO. Thus, to compensate for the impurity, an extra phase of NiO was added to our model. Figure 3.1a shows the Rietveld fit without adding the NiO phase and figure 3.1b shows the fit with extra phase. The region around the NiO (200) peak is expanded for sake of clarity. The figure 3.2 shows Rietveld refinement fit of the powder XRD pattern of $Ni_2AlO_2BO_3$.

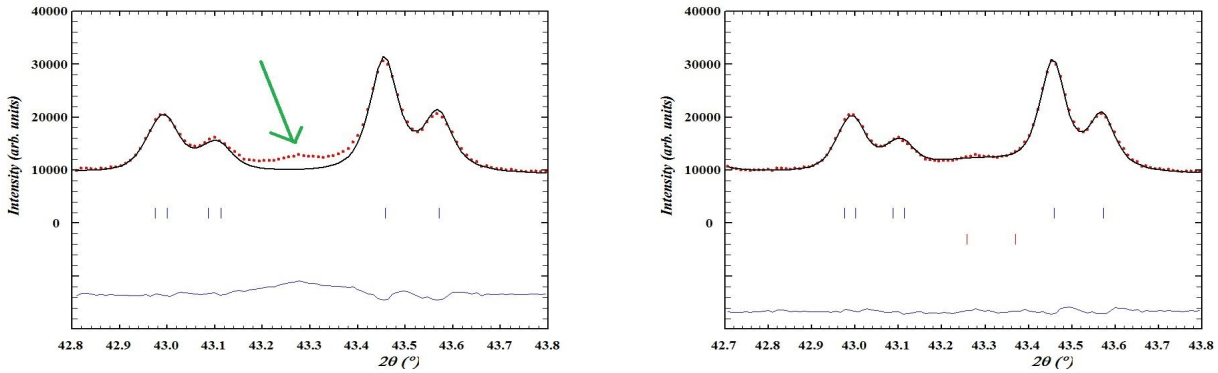

(a) (b)

Figure 3.1: Rietveld refinement fit (black line) of powder XRD pattern (red circles) of $Ni_2AlO_2BO_3$, Blue stripes indicate the peak positions of $Ni_2AlO_2BO_3$ Blue line is the difference in powder XRD and fitting (a) Impurity peak in XRD pattern (green arrow) (b) Impurity peak fitted with NiO, red strips are (200) peak of NiO

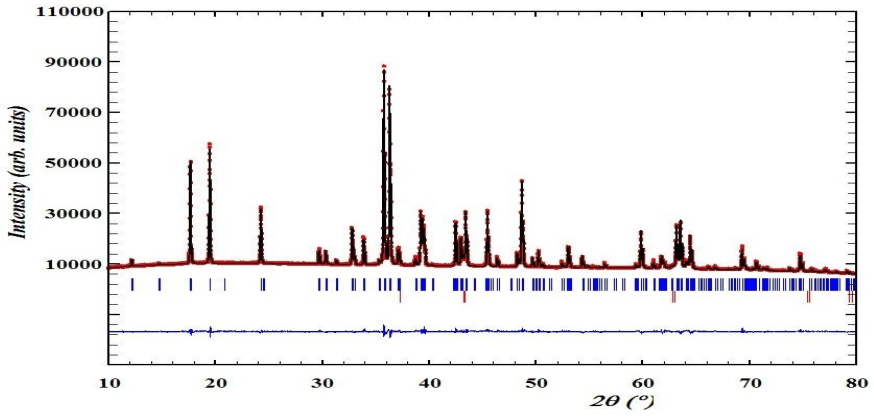

Figure 3.2: Rietveld refinement fit (black line) of powder XRD pattern (red circles) of $Ni_2AlO_2BO_3$, Blue and red stripes indicate the peak positions of $Ni_2AlO_2BO_3$ and NiO Blue line is the difference in data and our fit

Table 3.1: XRD data of $Ni_2AlO_2BO_3$

Chemical formula	Ni_2AlBO_5
Molecular weight, g/mol	235.17[6]
Temperature, K	296
Crystal Structure	Orthorhombic
Symmetry space group	*Pbam*
Unit cell parameters :	
a, Å	12.0137
b, Å	9.1059
c, Å	2.9419
α, β, γ, deg	90
V, Å^3	321.844
Diffraction angle θ, deg	5 - 39.9978
step size 2θ, deg	0.010380
R values:	
R_{wp}	6.45
R_e	3.81
Chi2	2.87
Goodness	1.69
Fraction of $Ni_2AlO_2BO_3$, %	97.92
Fraction of NiO, %	2.08

Rietveld refinement fit of $Ni_2AlO_2BO_3$ is shown in figure 3.2 with an extra phase of NiO to compensate for (200) impurity peak of NiO. The table 3.1 shows the parameters obtained from the diffraction data using Rietveld refinement fit of $Ni_2AlO_2BO_3$, also gives R values and percentage fraction of each phase. With addition of extra phase of NiO to incorporate for the impurity peak, it was calculated from the fit that 2.08% of sample is NiO. The fitting has a goodness of 1.69 which is in the acceptable range. The crystal structure is orthorhombic with *Pbam* crystal symmetry. To plot crystal structure Visualization for Electronic and STructural Analysis (VESTA) software was used [28]. The crystallographic structure projected along c direction is shown in figure 3.3 which matches with the general ludwigite structure shown in figure 1.1. Micron size crystals can be seen from the SEM images of $Ni_2AlO_2BO_3$ samples. The octahedral symmetry of the crystal structure can be seen in some of the crystals in figure 3.4.

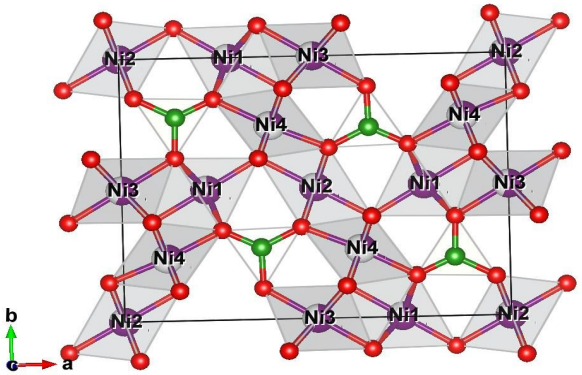

Figure 3.3: Crystal structure of $Ni_2AlO_2BO_3$ Violet/White atoms are metal ion positions with Ni (violet) and Al (white), projected along the crystallographic c direction, green atoms are boron ions and red are oxygen atoms

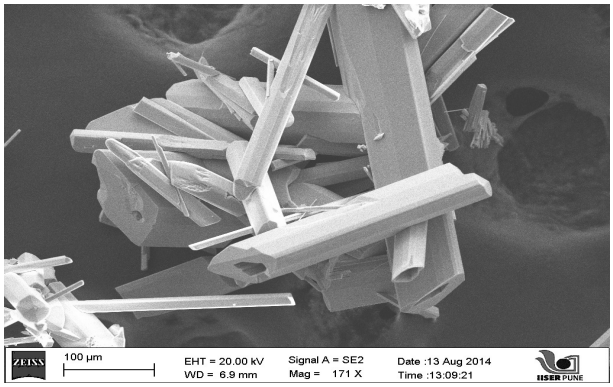

Figure 3.4: SEM image of $Ni_2AlO_2BO_3$

Table 3.2: Atomic positions and fractional occupancy in $Ni_2AlO_2BO_3$

Atom	x/a	y/b	z/c	Fractional occupancy
Ni1	0.28128	0.99699	0.5	0.80964
Al1	0.28128	0.99699	0.5	0.19036
Ni2	0	0	0.5	0.78504
Al2	0	0	0.5	0.21496
Ni3	0	0.5	0	0.56672
Al3	0	0.5	0	0.43328
Ni4	0.11401	0.2375	0	0.29634
Al4	0.11401	0.2375	0	0.70366
B1	0.35773	0.27409	0	1
O1	0.46308	0.34979	0	1
O2	0.14442	0.11376	0.5	1
O3	0.36098	0.11921	0	1
O4	0.07701	0.37747	0.5	1
O5	0.2577	0.34134	0	1

The atomic positions and fractional occupancy of atoms are given in table 3.2. The last digit in atomic positions and the last two digits in the fractional occupancy are uncertain. As mentioned in section 1.1.1 we have four different crystallographic metal ion positions with +3 and +2 ions occupied in all the four positions. The fractional occupancy of Al ions vary at different metal ion sites. Al^{3+} ions are occupied mostly at crystallographic site 4 and the least is at site 1. This pattern varies from the predicted pattern in [3] where the 3+ symmetric metal ion occupancy is maximum at site 4 and then 2 and the least occupied at sites 3 and 1. But from the table 3.2 we can see that the site 2 and 1 are least occupied and site 4 and 3 are more preferred by Al ions.

3.1.2 Magnetic properties of $Ni_2AlO_2BO_3$

Magnetic measurements of this sample was done using SQUID magnetometer. Zero field cooled (ZFC) and field cooled (FC) measurements were done at 100 Oe on $Ni_2AlO_2BO_3$ which shows a sharp transition at 38K which can be seen in figure 3.5. There is a splitting in the ZFC-FC curves of the sample near the magnetic transition. The correlations below transition temperature is antiferromagnetic in nature which is indicated by a drop in ZFC magnetization curve. At very low temperatures around 5K there is a small anomaly in ZFC and FC curves.

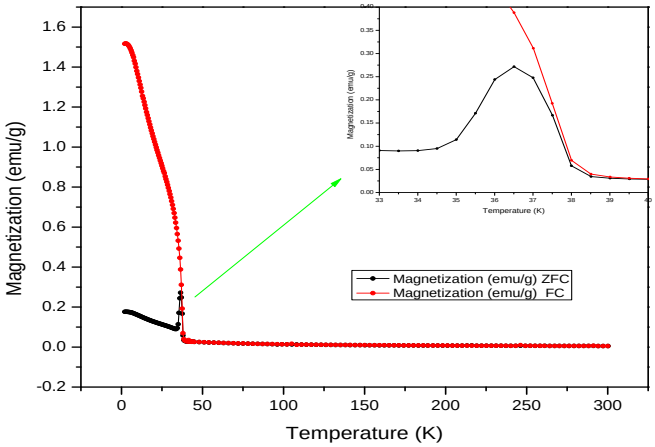

Figure 3.5: ZFC and FC measurement of $Ni_2AlO_2BO_3$ done at 100 Oe (Inset shows the enlarged view around transition temperature)

Figure 3.6 shows a plot of the inverse susceptibility versus temperature, and we can see that in the high temperature regime, the material behave as paramagnetic in nature. The linearity of the $\frac{1}{\chi}$ is not preserved till the transition temperature. The plot seems to deviate from the actual linear behavior below 180K which is around 5 times above the actual transition temperature of 38K. This behavior is quite often seen in compounds where there are short range correlations above the transition temperature. Some of the common examples are $La_{1-x}Ca_xMnO_3$ [29], $Tb_5Si_2Ge_2$ [30] etc.

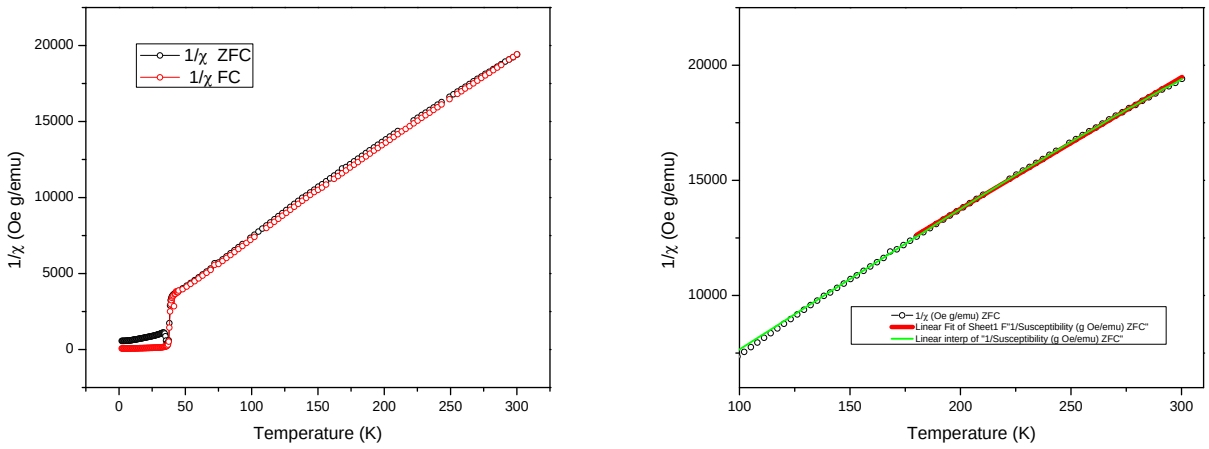

(a) (b)

Figure 3.6: (a) $1/\chi$ versus temperature plot of ZFC and FC measurement of $Ni_2AlO_2BO_3$ (b) $1/\chi$ plot for ZFC measurement of $Ni_2AlO_2BO_3$ with linear fitting (red line) from 180K to 300K (fitting parameters shown in table) and interpolated (green line).

The paramagnetic regime of $Ni_2AlO_2BO_3$ is fitted with Curie Weiss law and the fitting is shown in figure 3.6b. The linear fitting is done from 180K to 300K. The fitting parameters are shown in table 3.3.

Table 3.3: Linear fitting parameters in the paramagnetic region of $Ni_2AlO_2BO_3$ from 180K to 300K

Intercept		Slope		Statistics
Value	Error	Value	Error	Adj. R-Square
2.36×10^3	46.51	57.09	0.19	0.99

The Curie constant and Θ_c can be calculated from the fitting parameters

$$C = \frac{1}{slope} = 17.51 \times 10^{-3} \frac{g}{cm^3.K} \tag{3.1}$$

$$\Theta_c = -\frac{y\ intercept}{slope} = -41.11K \tag{3.2}$$

$$\frac{\mu_{eff}}{f.u} = \sqrt{\frac{3kCM'}{A}} \tag{3.3}$$

where:

M' = Molecular weight of $Ni_2AlO_2BO_3$ = 235.1763 g/mol,
k = Boltzmann Constant 1.3806 $\times$ 10^{-16} erg/K,
C = Curie Constant 17.51$\times10^{-3}$ g/(cm^3. K) and
A = Avogadro Number 6.0221 $\times$ 10^{23} mol^{-1}

Calculating effective magnetic moment per formula unit from equation 3.3

$$\frac{\mu_{eff}}{f.u} = 5.74\mu_B \tag{3.4}$$

$$\frac{\mu_{eff}}{Ni^{2+}ion} = 2.87\mu_B \tag{3.5}$$

The above calculated value of the magnetic moment of Ni^{2+} ion matches with theoretically calculated value which is 2.8284 μ_B in table 1.1. Thus both the Ni^{2+} ions contributes to the magnetic moment in the system. NiO orders antiferromagnetically at 520K, hence the contribution of the NiO impurity in the magnetization of $Ni_2AlO_2BO_3$ is negligible. The Θ_c calculated from the fitting is -41.12K which refers to the fact that the predominant correlations are antiferromagnetic in nature.

Magnetization versus field measurements were done at 5K from -7T to +7T. This measurement shows hysteresis behavior with a very small loop opening and a metamagnetic transition around 2T. This type of hysteresis behavior is common to weak ferromagnets. Figure 3.7b shows χ versus field plot of the virgin curve of hysteresis loop in $Ni_2AlO_2BO_3$ at 5K which shows a gradual change in susceptibility around 2T. The change in susceptibility is a clear signature of metamagnetic transition in $Ni_2AlO_2BO_3$. Metamagnetism is a first order magnetic phase transition where under the application of magnetic field, antiferromagnets show a change in magnetic moment [31]. These kind of transitions are not very uncommon for ludwigites systems. For example $Mn_{1.2}Ni_{1.8}O_2BO_3$ [32] and $Co_{2.4}Ga_{0.6}O_2BO_3$ [3] shows field driven transitions which can be seen as a clear jump in susceptibility. One such example is given in introduction section 1.1.3 figure 1.7b for $Co_{2.4}Ga_{0.6}O_2BO_3$. Our measurements reconfirm that the metamgnetic transition appear to be a feature of most hetrometallic ludwigites.

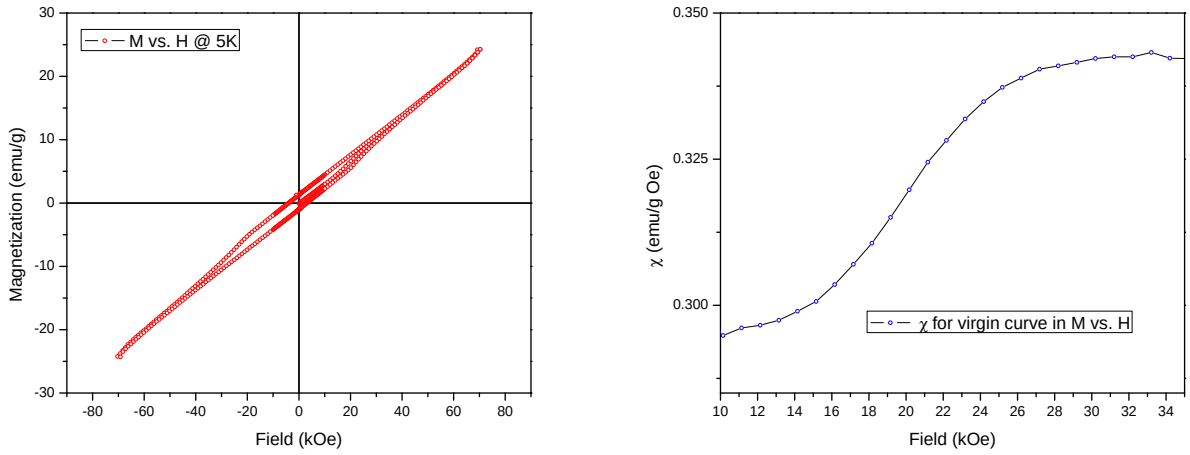

(a) (b)

Figure 3.7: (a) Magnetization versus Field at 5K for $Ni_2AlO_2BO_3$ (b) χ versus field plot of virgin magnetization isotherm of $Ni_2AlO_2BO_3$ which shows a metamagnetic transition around 2T.

3.1.3 Specific heat measurements of $Ni_2AlO_2BO_3$

Heat capacity measurements were done for $Ni_2AlO_2BO_3$ which showed a clear transition at 38K. Specific heat measurements were also done at 3T and 5T magnetic field across the transition temperature. The figure 3.8 shows the specific heat variation with respect to temperature and the inset shows the change in specific heat across the transition temperature at different magnetic fields. By increasing the magnetic field, we observe a suppression of the specific heat around the transition temperature. This large change in specific heat across transition temperature is an indication of a structural transition in the material at 38K. This structural transition is accompanied with a magnetic transition

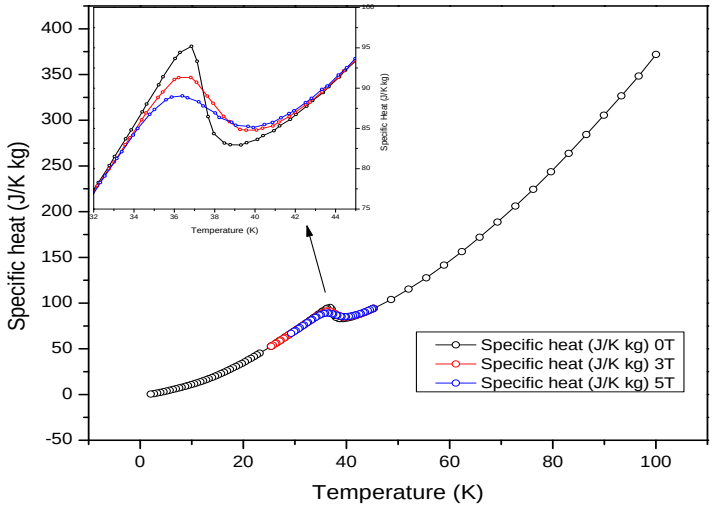

Figure 3.8: Specific heat variation with temperature in $Ni_2AlO_2BO_3$ at different applied magnetic fields (0, 3 & 5T) (Inset shows the transition temperature range)

from paramagnetic to antiferromagnetic phase. This phenomenon of temperature dependent magneto-structural transition are of great interest, and some of the recent materials which show such transitions are $Gd_5(Si_{0.1}Ge_{0.9})_4$ [33], $Ca_{0.85}Sm_{0.15}MnO_3$ [34] etc. When magnetic field is applied the peak in specific heat shifts to a lower temperature seen in inset of figure 3.8.

Form basic solid state physics we know that the major contributors to the specific heat are from electrons and phonons. The phonon contribution to the specific heat at low temperature varies as cube of the temperature while the electronic contribution is linear in nature [17]. This is depicted in equation 3.6, where αT is the specific heat contribution due to free electrons in the material and βT^3 is from phonons. Thus if a plot of specific heat scaled with temperature $\left(\frac{C}{T}\right)$ is plotted against the square of temperature, we expect a linear behavior at very low temperatures, with α as the y intercept and β as the slope of the curve.

$$C = \alpha T + \beta T^3 \tag{3.6}$$

$\frac{C}{T}$ versus T^2 plot for $Ni_2AlO_2BO_3$ at low temperature zero magnetic field data does not follow the above described linear relationship. The inset of figure 3.9 shows this anomaly at the low temperature regime. This anomaly could be due to a magnetic transition at lower temperature which was also observed in the ZFC-FC measurements of $Ni_2AlO_2BO_3$. To analyze the contribution of magnetic part to the specific heat at low temperature, first the phononic contribution has to be subtracted. Since the compound is assumed to be insulator, the electronic contribution can be neglected. To do a more rigorous analysis of this low temperature magnetic transition we have to find the phonon contribution from other nonmagnetic ludwigites with similar structural properties.

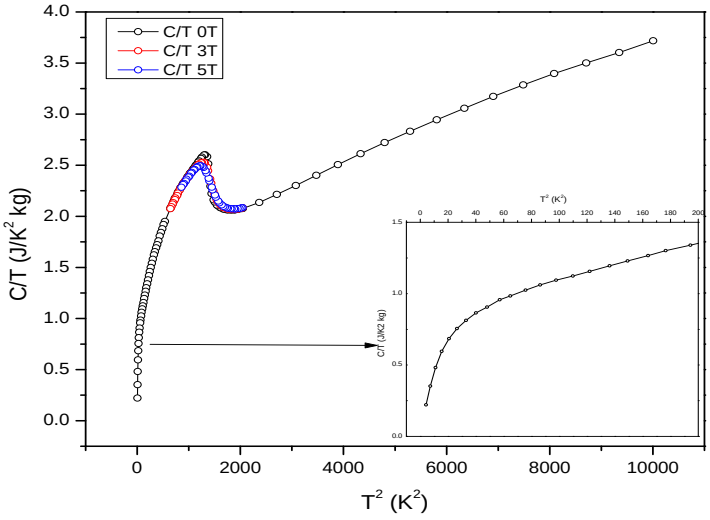

Figure 3.9: C/T versus T^2 plot of $Ni_2AlO_2BO_3$ at 0, 3 and 5T magnetic fields (Inset shows the low temperature data at 0T, which does not follow linear behavior at low temperature)

3.1.4 MCE in $Ni_2AlO_2BO_3$

The suppression of specific heat with magnetic fields clearly indicate that there would be an entropy change in the material in the vicinity of the above transition.

To calculate this, first heat capacity was measured and then converted to specific heat and divided by the respective temperature. This $\frac{C(T)_{P,H}}{T}$ was integrated with respect to temperature using the Origin software. To find the entropy change, we used entropy at zero magnetic field as a reference data, which was subtracted from all the other measurements at nonzero magnetic fields 3.7.

$$\Delta S(T)_{\Delta H} = \int_0^T \frac{C(T)_{P,H\neq 0}}{T} dT - \int_0^T \frac{C(T)_{P,H=0}}{T} dT \tag{3.7}$$

The entropy change in $Ni_2AlO_2BO_3$ was calculated using the equation 3.7. As mentioned in section 1.3 we can see from figure 3.10 a maximum entropy change at the transition temperature. Also entropy change is negative for a given positive magnetic field. Aside from the general features, the maximum of entropy change shows a slight shift towards higher temperature when the magnetic field is increased. The entropy is increased while applying higher magnetic fields which is also observed as an increase is entropy change for higher magnetic fields. This large change in entropy gives further evidence that the transition observed at 38K is a first order transition with a coincident magnetic and a probable structural transition.

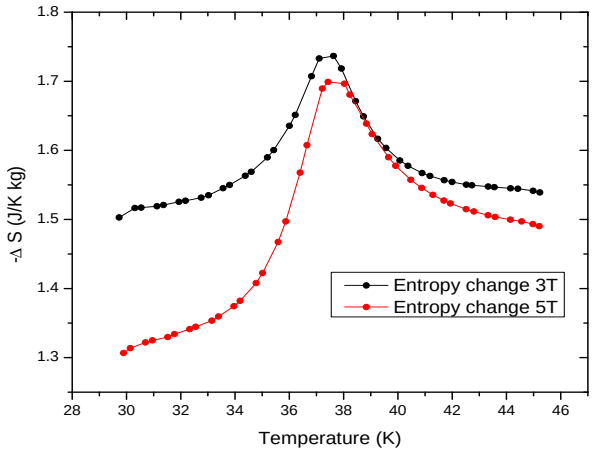

Figure 3.10: Entropy change (MCE) in $Ni_2AlO_2BO_3$ around the transition temperature

3.1.5 Dielectric spectroscopy measurements of $Ni_2AlO_2BO_3$

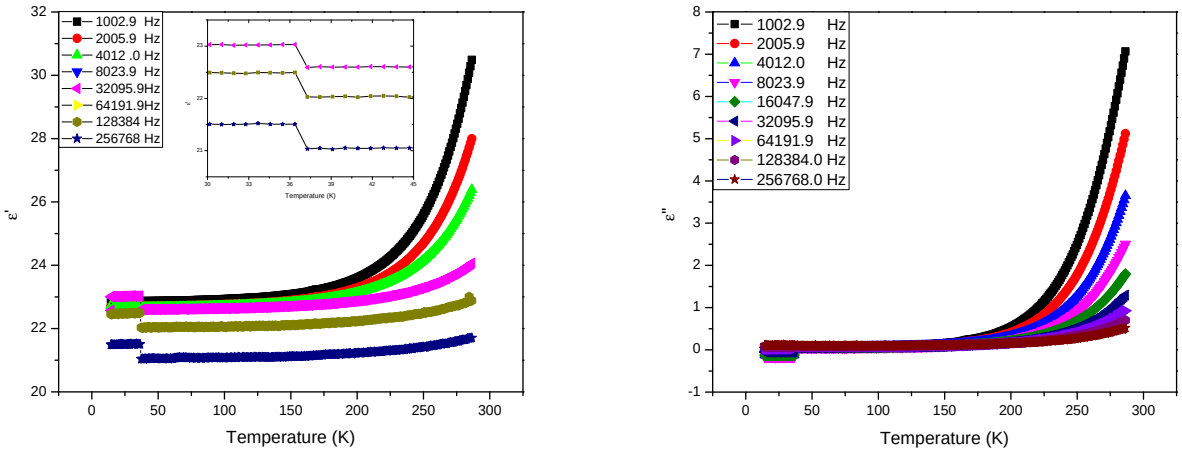

(a) (b)

Figure 3.11: (a) Real part (ϵ') (inset shows the jump in ϵ' around transition temperature for selected frequencies) (b) Imaginary part (ϵ") of dielectric constant of $Ni_2AlO_2BO_3$ shows a transition at 38K.

Temperature versus real and imaginary parts of dielectric constant were measured for different frequencies. Dielectric constant of $Ni_2AlO_2BO_3$ shows a sudden jump at 38K where there is a magnetic transition figure 3.11. This sudden jump in dielectric constant is an indication of a structural transition in the material. Since there is a magnetic transition along with a sudden change in dielectric constant, this transition could be magnetodielectric in nature. One of such example was $Ni_3V_2O_8$ discussed in

introduction section 1.2.2 where there is a sudden jump in dielectric constant across a magnetic transition temperature [13]. This sudden change can be seen both in the real and imaginary parts of the dielectric constant.

3.2 $Co_2AlO_2BO_3$

3.2.1 Structural analysis of $Co_2AlO_2BO_3$

Rietveld refinement of $Co_2AlO_2BO_3$ was performed, and the given phase was pure within the detection limits of XRD. The crystal structure and the symmetry space group matches with the general ludwigite structure. The figure 3.12 shows Rietveld refinement fit of the powder XRD pattern of $Co_2AlO_2BO_3$.

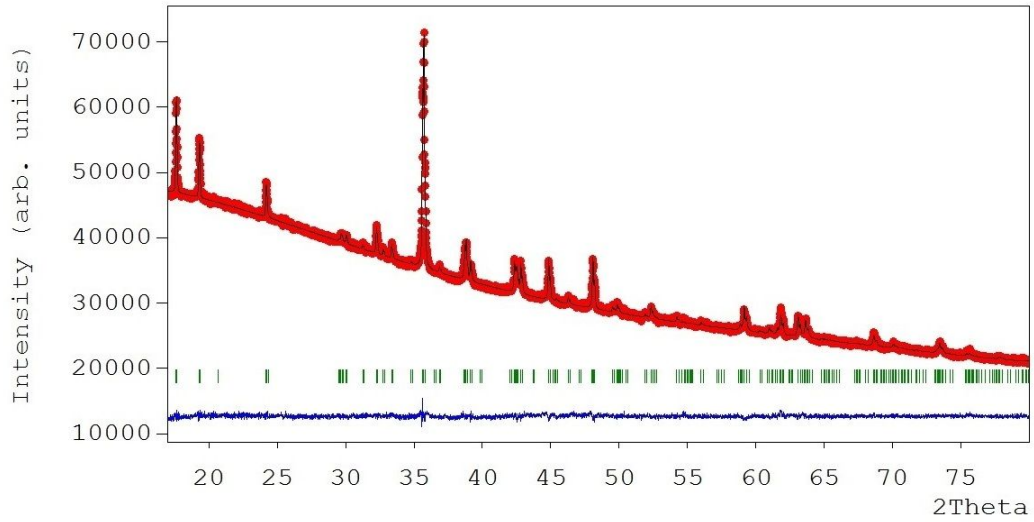

Figure 3.12: Rietveld refinement fit (black line) of powder XRD pattern (red circles) of $Co_2AlO_2BO_3$, green stripes indicate the peak positions of $Co_2AlO_2BO_3$, Blue line is the difference in data and our fit.

The table 3.4 shows the diffraction data obtained from Rietveld refinement fit of $Co_2AlO_2BO_3$, and also gives R values. The goodness of fit is 1.25 which is in the acceptable range. The sample shows orthorhombic crystal structure with *Pbam* symmetry space group. The crystal structure projected on 001 crystallographic direction is shown in figure 3.13. This structure is similar to what has been observed in $Ni_2AlO_2BO_3$ and in other ludwigites. Atomic positions and fractional occupancy of atomic sites are given in table 3.5. The last two digits in the fractional occupancy are uncertain. There are four different crystallographic metal ion positions with occupancy of both +2 and +3 ions in each site. Site 2 has the least occupancy of Al ions while site 4 has the maximum occupancy.

Table 3.4: XRD data of $Co_2AlO_2BO_3$

Chemical formula	Co_2AlBO_5
Molecular weight, g/mol	235.65[6]
Temperature, K	296
Crystal Structure	Orthorhombic
Symmetry space group	*Pbam*
Unit cell parameters :	
a, Å	12.0349
b, Å	9.2009
c, Å	2.9978
α, β, γ, deg	90
V, Å^3	331.946
Diffraction angle θ, deg	8.5034 - 39.9978
step size 2θ, deg	0.010380
R values:	
R_{wp}	15.0
R_e	12.0
Chi2	1.56
Goodness	1.25

Table 3.5: Atomic positions and fractional occupancy in $Co_2AlO_2BO_3$

Atom	x/a	y/b	z/c	Fractional occupancy
Co1	0.2752(2)	0.9985(7)	0.5	0.69166
Al1	0.2752(2)	0.9985(7)	0.5	0.30834
Co2	0	0	0.5	0.86516
Al2	0	0	0.5	0.13484
Co3	0	0.5	0	0.54968
Al3	0	0.5	0	0.45032
Co4	0.1144(5)	0.2357(5)	0	0.4578
Al4	0.1144(5)	0.2357(5)	0	0.5422
B1	0.373(4)	0.256(3)	0	1
O1	0.4596(10)	0.3610(12)	0	1
O2	0.1354(14)	0.1204(10)	0.5	1
O3	0.3572(14)	0.1284(10)	0	1
O4	0.0735(11)	0.3972(9)	0.5	1
O5	0.2576(11)	0.3328(13)	0	1

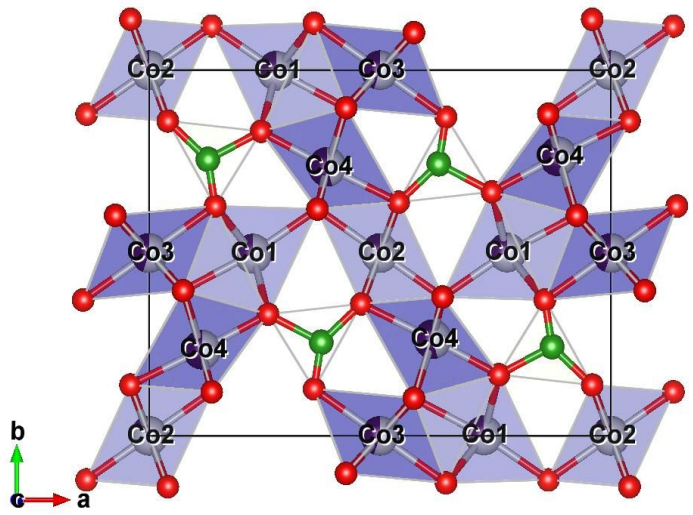

Figure 3.13: Crystal structure of $Co_2AlO_2BO_3$ Gray/black atoms are metal ion positions with Co (gray) and Al (black) projected along crystallographic c direction, green atoms are boron ions and red are oxygen atoms

Table 3.6: Percentage occupancy of metal ion sites in $Co_2AlO_2BO_3$ & $Ni_2AlO_2BO_3$

$Co_2AlO_2BO_3$		**$Ni_2AlO_2BO_3$**	
Metal ion site	Percentage occupancy %	Metal ion site	Percentage occupancy %
Co1	69.166	Ni1	80.964
Al1	30.834	Al1	19.036
Co2	86.516	Ni2	78.504
Al2	13.484	Al2	21.496
Co3	54.968	Ni3	56.672
Al3	45.032	Al3	43.328
Co4	45.78	Ni4	29.634
Al4	54.22	Al4	70.366

Table 3.6 shows the percentage occupancy in different metal ion sites in $Co_2AlO_2BO_3$ and $Ni_2AlO_2BO_3$. Aluminum ions clearly prefer metal ion site 4 in both $Ni_2AlO_2BO_3$ and $Co_2AlO_2BO_3$. Site 3 has approximately the same preference for 3+ ions in both the compounds. In $Ni_2AlO_2BO_3$, aluminum ions are least occupied at site 1 while in

$Co_2AlO_2BO_3$ it is site 2. Thus the occupancy pattern of 3+ ions differs slightly from what has been reported for $Co_{2.6}Ga_{0.4}O_2BO_3$ [3] which claims that site site 4 has the highest occupancy of 3+ ion while site 1 and 3 has the least. But in our case site 1 and 2 are the least occupant sites of 3+ ions while site 4 remains with the highest occupant site of 3+ ions.

3.2.2 Magnetic properties of $Co_2AlO_2BO_3$

Zero field cooled (ZFC) and field cooled (FC) measurements were done on powdered $Co_2AlO_2BO_3$ sample at 100 Oe. The ZFC measurement indicates that the sample has an antiferromagnetic transition, but it is not as sharp as what is being observed in $Ni_2AlO_2BO_3$. The maximum of the ZFC curve is at 27K. There is a clear splitting of the ZFC and FC from 36K onwards which can be seen in the inset of figure 3.14 indicated by orange arrow. Since the transition is smeared no clear transition temperature can be defined using magnetic measurements alone.

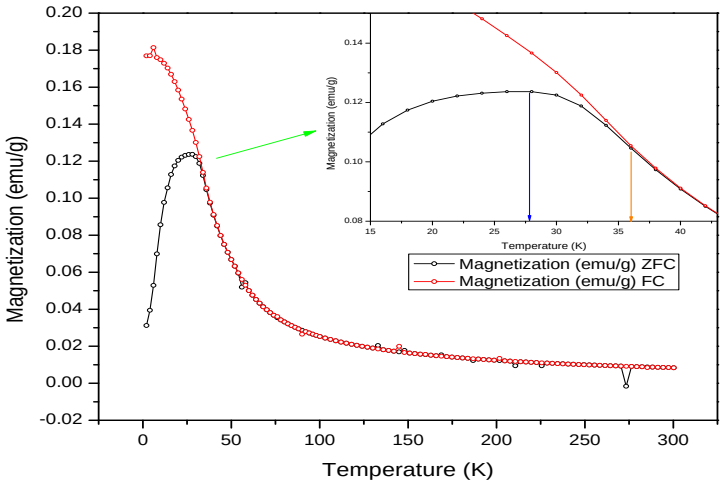

Figure 3.14: ZFC and FC curves of $Co_2AlO_2BO_3$ done at 100 Oe inset shows the transition temperature range, maxima of ZFC curve (Blue arrow at 27K) and splitting of ZFC-FC curve (orange arrow at 36K)

The inverse susceptibility of ZFC and FC curves completely overlaps in the paramagnetic region. But the linearity of inverse susceptibility is not preserved till the splitting of the ZFC and FC curves. Thus as mentioned in the earlier case of $Ni_2AlO_2BO_3$ there could be short range correlations above the transition temperature till 130K which is 3.5 times above the magnetic transition temperature. The linear region of the inverse susceptibility curve of the ZFC curve was fitted with Curie-Weiss law. Fitting parameters are shown in table 3.7.

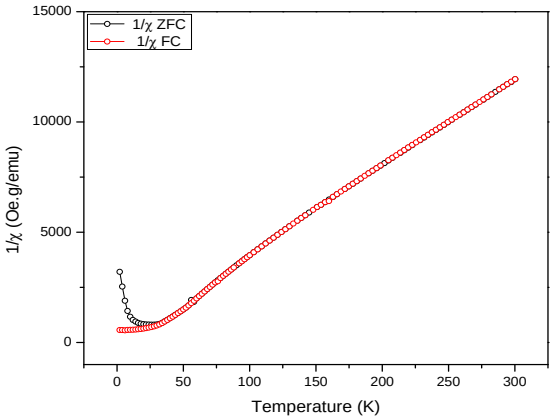

(a)

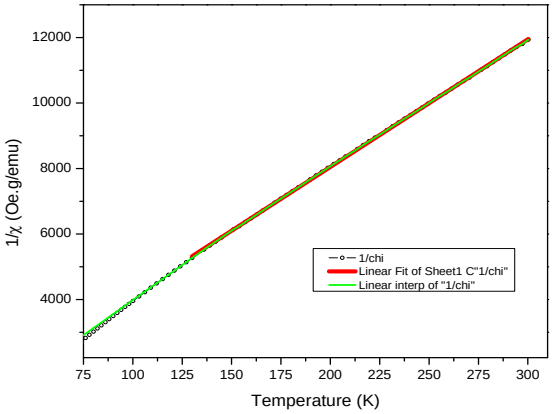

(b)

Figure 3.15: (a) $1/\chi$ versus temperature plot of ZFC and FC measurement of $Co_2AlO_2BO_3$ (b) $1/\chi$ plot for ZFC measurement of $Co_2AlO_2BO_3$ with linear fitting (red line) from 130K to 300K (fitting parameters shown in table) and interpolated (green line)

Table 3.7: Linear fitting parameters in the paramagnetic region of $Co_2AlO_2BO_3$ from 130K to 300K

Intercept		Slope		Statistics
Value	Error	Value	Error	Adj. R-Square
2.57×10^2	10.19	38.95	0.05	0.99

The Curie constant and Θ_c can be calculated from the fitting parameters

$$C = \frac{1}{slope} = 25.66 \times 10^{-3} \frac{g}{cm^3.K} \tag{3.8}$$

$$\Theta_c = -\frac{y\ intercept}{slope} = -6.59K \tag{3.9}$$

$$\frac{\mu_{eff}}{f.u} = \sqrt{\frac{3kCM'}{A}} \tag{3.10}$$

where:

M' = Molecular weight of $Co_2AlO_2BO_3$ = 235.6559 g/mol,
k = Boltzmann Constant 1.3806×10^{-16} erg/K,
C = Curie Constant 25.66×10^{-3} g/(cm^3. K) and
A = Avogadro Number 6.0221×10^{23} mol^{-1}

Calculating effective magnetic moment per formula unit from equation 3.10

$$\frac{\mu_{eff}}{f.u} = 6.96\mu_B \tag{3.11}$$

$$\frac{\mu_{eff}}{Co^{2+}ion} = 3.48\mu_B \tag{3.12}$$

The above calculated value of the magnetic moment of Co^{2+} ion approximately matches with the theoretically calculated value which is 3.8730 μ_B from table 1.1. Thus both of the Co^{2+} ion contributes to the magnetic properties in the system. This also proves that the cobalt is in high spin state in $Co_2AlO_2BO_3$. Otherwise the effective magnetic moment of per cobalt ion would have been 1.7321 μ_B. The Θ_c calculated from the fitting is -6.5896K which refers to the fact that there is antiferromagnetic correlations below transition temperature. Thus we observe in both alumino-ludwigites, an antiferromagnetic transition with transition temperatures 38K for $Ni_2AlO_2BO_3$ and 36K for $Co_2AlO_2BO_3$. The present ludwigite shows antiferromagnetic behavior at low temperature matches with $Co_{2.6}Ga_{0.4}O_2BO_3$ [3] where there is an antiferromagnetic transition temperature at 37K.

3.2.3 Specific heat measurements of $Co_2AlO_2BO_3$

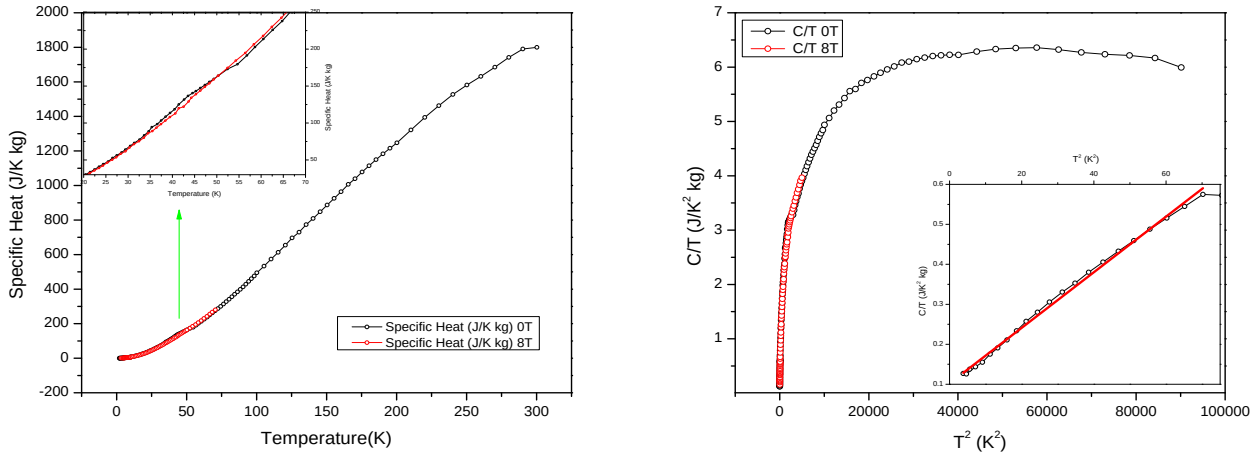

(a) (b)

Figure 3.16: (a) Specific heat versus temperature plot of $Co_2AlO_2BO_3$ with 0T and 8T magnetic fields (b) C/T vs. T^2 of $Co_2AlO_2BO_3$ at 0T and 8T (Inset shows the low temperature data at 0T fitted with linear curve (red))

Heat capacity measurements were done for $Co_2AlO_2BO_3$ at 0T and 8T magnetic field. The figure 3.16a shows specific heat versus temperature plot and inset shows the transition temperature region. The inset of figure 3.16a shows a change in specific heat

around 50K in $Co_2AlO_2BO_3$. There is an observable difference in specific heat across the magnetic transition temperature (36K) between 0T and 8T. The change in specific heat around 50K could mean that there is a transition which is not magnetic in nature. The C/T versus T^2 shows approximate linear behavior at very low temperature range (2K - 8.5K) which is expected from basic understanding of specific heat. The equation which is followed by specific heat at low temperature is given by equation 3.6 which was discussed in earlier. The linear fit at low temperature region is shown in the inset of figure 3.16b with the fitting parameters in table. From the table 3.8 above fitting $\alpha = 0.10 JK^{-2}kg^{-1}$ and $\beta = 6.95 \times 10^{-3} JK^{-4}kg^{-1}$. The behavior is not observed in $Ni_2AlO_2BO_3$ because of a low temperature magnetic anomaly.

Table 3.8: Linear fitting parameters in low temperature region of C/T vs. T^2 in $Co_2AlO_2BO_3$

Intercept		Slope		Statistics
Value	Error	Value	Error	Adj. R-Square
0.10	3.08×10^{-3}	6.95×10^{-3}	8.48×10^{-5}	0.99

Isothermal heat capacity versus field was done at 2K and 8K for the $Co_2AlO_2BO_3$ sample. The figure 3.17 shows magnetic field dependence of specific heat. When magnetic field increases, there is a decrease in the specific heat which is due to the magnetocaloric effect. When the material undergoes a metamgnetic transition, there will be a change in the specific heat of the material which would be an observable anomaly in the isothermal specific heat versus magnetic field measurement.

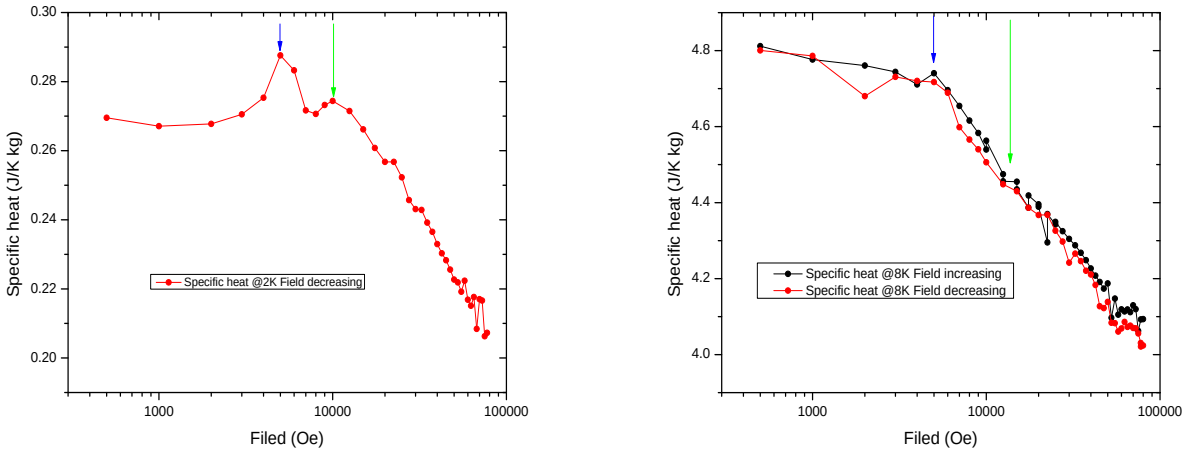

(a) (b)

Figure 3.17: Isothermal specific heat measurements of $Co_2AlO_2BO_3$ at (a) 2K, metamagnetic transition at 0.5T (blue arrow) and 1T(green arrow) (b) 8K, metamagnetic transition at 0.5T (blue arrow) and 1.2T (green arrow). x-axis is in $\log_{10}$ scale

Isothermal specific heat measured at 2K shows two transitions one at 0.5T and another at 1T which is indicated by blue arrow and green arrows in figure 3.17a. At 8K isothermal specific heat shows metamagnetic transition at 0.5T and 1.2T figure 3.17b which is indicating that the second meatmagnetic transition is highly temperature dependent. The x axis of both the graphs are plotted in $\log_{10}$ scale to see the transition more clearly. This transitions can be more clearly seen in magnetization versus field measurements of the sample where there will be a sharp jump in susceptibility across metamagnetic transition. This has been observed in $Ni_2AlO_2BO_3$ as we saw in earlier, but also in other hetrometallic ludwigites like cobalt gallium ludwigites [3] , manganese nickel ludwigites [32] etc.

3.2.4 MCE in $Co_2AlO_2BO_3$

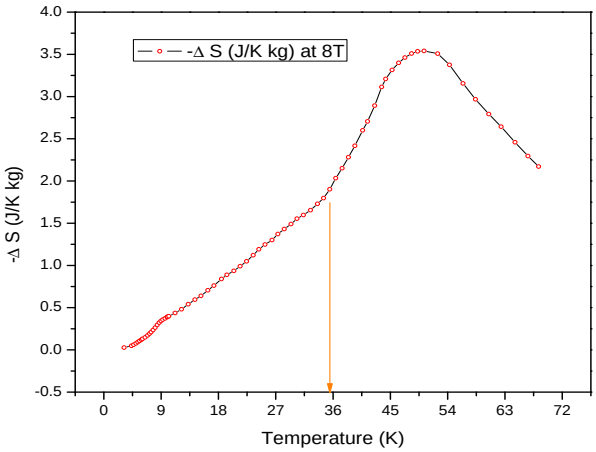

Figure 3.18: Entropy change (MCE) in $Co_2AlO_2BO_3$ with anomaly at 36K (orange arrow)

Entropy change was calculated for specific heat measured at field of 8T by equation 3.7. As mentioned earlier we can see a maximum change in entropy around the transition temperature 50K. Also entropy change is negative for a given positive magnetic field. But there is a change in the slope of specific heat curve at the magnetic transition temperature which is at 36K indicated by an orange arrow in figure 3.18. Careful observation of entropy change at lower temperature we can see an anomaly around 8K. Which is not reflected in any other measurements. Thus it is clear from the entropy change in the system that there is a first order phase transition at 50K which is only being reflected in the specific heat measurement. It is worth nothing that the change in entropy in two times higher than that of what has been observed in $Ni_2AlO_2BO_3$. Dielectric measurements of the sample does not show any anomaly at either of the transition temperatures.

3.3 Conclusions

$Co_2AlO_2BO_3$ and $Ni_2AlO_2BO_3$ have orthorhombic crystal structure with *Pbam* space group. There are 4 different crystallographic metal ion positions with varying occupancies of transition metal ion and aluminum ions. Site 4 has the maximum occupancy of +3 metal ion which is aluminum in our case, which matches with previous reports [3]. $Ni_2AlO_2BO_3$ shows an antiferromagnetic transition at 38K. This transition is clearly combined with a structural transition which is indicted in dielectric and specific heat measurements. Since there is a sudden jump in dielectric constant at the magnetic transition temperature. There is a possibility of magnetodielectric effect in $Ni_2AlO_2BO_3$ which has to be further investigated. Metamagnetic transition has been observed in M vs. H hysteresis measurement of $Ni_2AlO_2BO_3$ at 2T. MCE has also been observed in $Ni_2AlO_2BO_3$ across the transition temperature indicating a first order transition.

$Co_2AlO_2BO_3$ has an antiferromagnetic transition at 36K. The specific heat measurements of $Co_2AlO_2BO_3$ shows a possible first order transition at 50K which was not observed in magnetic or dielectric measurements. MCE in $Co_2AlO_2BO_3$ has a maximum at 50K (3.5 J/K kg) and an anomaly at 36K. MCE in $Co_2AlO_2BO_3$ is twice of what has been observed in $Ni_2AlO_2BO_3$. Indication of two metamagnetic transitions are there in isothermal specific heat measurements of $Co_2AlO_2BO_3$ at 8K and 2K.

3.4 Future Plans

- Magnetization versus field masurements are still to be done for $Co_2AlO_2BO_3$. Multiple metamagnetic transitions are possible in this material which is indicated by isothermal specific heat measurements.
- There is a clear indication of a structural transition in $Ni_2AlO_2BO_3$ from specific heat and dielectric measurements. Thus a low temperature XRD measurement is essential to confirm this structural transition.
- Further investigation is required for the low temperature anomaly of specific heat in $Ni_2AlO_2BO_3$. For subtracting the phonon contribution, a similar nonmagnetic ludwigite's specific heat data at low temperature is required. Synthesis of such a nonmagnetic ludwigite ($Mg_2AlO_2BO_3$) is under process. Calculation of magnetic contribution could be possible if the synthesis is successful.
- More measurements are required to characterize the first order transition at 50K in $Co_2AlO_2BO_3$. Low temperature XRD would be required to identify if there are any structural transitions.
- The magnetic transition in $Ni_2AlO_2BO_3$ is coupled with a jump in dielectric constant thus indicating the possibility of magnetodielectric effect. For the confirmation of magnetodielectric effect, dielectric measurement should be carried out in presence of varying magnetic field across this transition temperature.

References

[1] M. Continentino, J. Fernandes, R. Guimarães, B. Boechat, A. Saguia, Frontiers in Magnetic Materials, Springer Berlin Heidelberg, 2005, Ch. Magnetism in Highly Anisotropic Borates: Experiment and Theory, p. 385.

[2] Continentino, M.A. and Fernandes, J.C. and Guimaraes R. B., H. Borges, A. Sulpice, J.-L. Tholence, J. Siqueira, J. da Cunha, C. dos Santos, Magnetic interactions in the monoclinic ludwigite $Cu_2FeO_2BO_3$, The European Physical Journal B - Condensed Matter and Complex Systems 9 (1999) 613.

[3] N. B. Ivanova, M. S. Platunov, Y. V. Knyazev, N. V. Kazak, L. N. Bezmaternykh, A. D. Vasiliev, S. G. Ovchinnikov, V. I. Nizhankovskii, Effect of the diamagnetic dilution on the magnetic ordering and electrical conductivity in the $Co_3O_2BO_3$: Ga ludwigite, Physics of the Solid State 54 (2012) 2212.

[4] M. Mir, R. B. Guimarães, J. C. Fernandes, M. A. Continentino, A. C. Doriguetto, Y. P. Mascarenhas, J. Ellena, E. E. Castellano, R. S. Freitas, L. Ghivelder, Structural Transition and Pair Formation in $Fe_3O_2BO_3$, Phys. Rev. Lett. 87 (2001) 147201.

[5] P. Bordet, E. Suard, Magnetic structure and charge ordering in Fe_3BO_5: A single-crystal x-ray and neutron powder diffraction study, Phys. Rev. B 79 (2009) 144408.

[6] J. Larrea J., D. R. Sánchez, F. J. Litterst, E. M. Baggio-Saitovitch, J. C. Fernandes, R. B. Guimarães, M. A. Continentino, Magnetism and charge ordering in $Fe_3O_2BO_3$ studied by ^{57}Fe Mössbauer spectroscopy, Phys. Rev. B 70 (2004) 174452.

[7] J. van den Brink, D. I. Khomskii, Multiferroicity due to charge ordering, Journal of Physics: Condensed Matter 20 (2008) 434217.

[8] Kimura, T. Goto, T. Shintani, H. Ishizaka, K. Arima, T. Tokura, Y., Magnetic control of ferroelectric polarization, Nature 426 (2003) 55.

[9] Eerenstein, W. Mathur, N. D. Scott, J. F., Multiferroic and magnetoelectric materials, Nature Reviews 422 (2006) 759.

[10] T. Kimura, Spiral Magnets as Magnetoelectrics, Annual Review of Materials Research 37 (1) (2007) 387.

[11] Bas B. Van Aken, Thomas T.M. Palstra, Alessio Filippetti and Nicola A. Spaldin, The origin of ferroelectricity in magnetoelectric $YMnO_3$, Nature materials 3 (2004) 164.

[12] F. C. i Fernàndez, Magnetocaloric Effect In $Gd_5(Si_xGe_{1-x})4$ Alloys, Ph.D. thesis, Universitat de Barcelona (España) (2004).

[13] G. Lawes, T. Kimura, C. Varma, M. Subramanian, N. Rogado, R. Cava, A. Ramirez, Magnetodielectric effects at magnetic ordering transitions, Progress in Solid State Chemistry 37 (2009) 40.

[14] H. Schmid, Some symmetry aspects of ferroics and single phase multiferroics, Journal of Physics: Condensed Matter 20 (2008) 434201.

[15] G. Lawes, A. P. Ramirez, C. M. Varma, M. A. Subramanian, Magnetodielectric Effects from Spin Fluctuations in Isostructural Ferromagnetic and Antiferromagnetic Systems, Phys. Rev. Lett. 91 (2003) 257208.

[16] V. K. Pecharsky, K. A. G. Jr, Magnetocaloric effect and magnetic refrigeration, Journal of Magnetism and Magnetic Materials 200 (1999) 44.

[17] Charles Kittel, Introduction to solid state physics, Wiley, 1991.

[18] J. Hriljac, R. Brown, A. Cheetham, L. Satek, The synthesis and crystal structures of the related series of aluminoborates: $Co_{2.1}Al_{0.9}BO_5$, Ni_2AlBO_5, and Cu_2AlBO_5, Journal of Solid State Chemistry 84 (1990) 289.

[19] K. Bluhm, H. Müller-Buschbaum, Ein Beitrag über Oxometallate mit trigonal planaren BO_3 -Polyedern Ni_2MBO_5 (M = Ga, Fe, Al, Cr), Zeitschrift für anorganische und allgemeine Chemie 582 (1990) 15.

[20] H. M. Rietveld, A profile refinement method for nuclear and magnetic structures, Journal of Applied Crystallography 2 (1969) 65.

[21] R. A. Young, The Rietveld Method, Oxford University Press, 1995.

[22] FullProf Suite (February 2016).

[23] R. L. Fagaly, Superconducting quantum interference device instruments and applications, Review of Scientific Instruments 77 (2006) 101101.

[24] B. D. Josephson, Possible new effects in superconductive tunnelling, Physics Letters 1 (1962) 251.

[25] G. E. Johnstone, Neutron and X-ray Scattering Study of Magnetic Manganites, Ph.D. thesis, Mansfield College, University of Oxford (2012).

[26] P. Freeman, Magnetism and the Magnetic Excitations of Charge Ordered $La_{2-x}Sr_xNiO_{4+\delta}$, Ph.D. thesis, Department of Physics, University of Oxford (2005).

[27] K. Mishra, Investigation of Physical properties of Pyrochlore Iridiates, Master's thesis, Indian Institute of Science Education and Research, Pune (May 2015).

[28] Visualization for Electronic and STructural Analysis (VESTA), version 3.3.2 Edition (Nov 12 2015).

[29] W. t. Jiang, Is a Griffiths Phase a Prerequisite for Colossal Magnetoresistance?, Phys. Rev. Lett. 99 (2007) 177203.

[30] C. Magen, P. A. Algarabel, L. Morellon, J. P. Araújo, C. Ritter, M. R. Ibarra, A. M. Pereira, J. B. Sousa, Observation of a Griffiths-like Phase in the Magnetocaloric Compound $Tb_5Si_2Ge_2$, Phys. Rev. Lett. 96 (2006) 167201.

[31] E. Stryjewski, N. Giordano, Metamagnetism, Advances in Physics 26 (1977) 487.

[32] L. Bezmaternykh, E. Kolesnikova, E. Eremin, S. Sofronova, N. Volkov, M. Molokeev, Magnetization pole reversal of ferrimagnetic ludwigites $Mn_{3-x}Ni_xBO_5$, Journal of Magnetism and Magnetic Materials 364 (2014) 55.

[33] L. Morellon, J. Blasco, P. A. Algarabel, M. R. Ibarra, Nature of the first-order antiferromagnetic-ferromagnetic transition in the Ge-rich magnetocaloric compounds $Gd_5(Si_xGe_{1-x})_4$, Phys. Rev. B 62 (2000) 1022.

[34] Filippov, D. A. and Levitin, R. Z. and Vasil'ev, A. N. and Voloshok, T. N. and Kageyama, H. and Suryanarayanan, R., Spontaneous and field-induced magnetostructural transitions, giant magnetostriction, and specific heat in $Ca_{0.85}Sm_{0.15}MnO_3$, Phys. Rev. B 65 (2002) 100404.

[35] N. V. Kazak, N. B. Ivanova, V. V. Rudenko, A. D. Vasil'ev, D. A. Velikanov, S. G. Ovchinnikov, Low-field magnetization of ludwigites $Co_3O_2BO_3$, Physics of the Solid State 51 (2009) 966–969.

[36] J. C. Fernandes, R. B. Guimarães, M. A. Continentino, H. A. Borges, A. Sulpice, J.-L. Tholence, J. L. Siqueira, L. I. Zawislak, J. B. M. da Cunha, C. A. dos Santos, Magnetic interactions in the ludwigite $Ni_2FeO_2BO_3$, Phys. Rev. B 58 (1998) 287–292.

[37] J. Bartolomé, A. Arauzo, N. V. Kazak, N. B. Ivanova, S. G. Ovchinnikov, Y. V. Knyazev, I. S. Lyubutin, Uniaxial magnetic anisotropy in $Co_{2.25}Fe_{0.75}O_2BO_3$ compared to $Co_3O_2BO_3$ and Fe_3O_2BO ludwigites, Phys. Rev. B 83 (2011) 144426.

[38] N. B. Ivanova, N. V. Kazak, Y. V. Knyazev, D. A. Velikanov, L. N. Bezmaternykh, S. G. Ovchinnikov, A. D. Vasiliev, M. S. Platunov, J. Bartolomé, G. S. Patrin, Crystal structure and magnetic anisotropy of ludwigite $Co_2FeO_2BO_3$, Journal of Experimental and Theoretical Physics 113 (2012) 1015.

[39] G. A. Petrakovskiĭ, L. N. Bezmaternykh, D. A. Velikanov, A. M. Vorotynov, O. A. Bayukov, M. Schneider, Magnetic properties of single crystals of ludwigites Cu_2MBO_5 (M = Fe^{3+}, Ga^{3+}), Physics of the Solid State 10 (2009) 2077.

[40] G. A. Petrakovskiĭ, L. N. Bezmaternykh, D. A. Velikanov, M. S. Malokeev, O. A. Bayukov, A. M. Vorotynov, R. Szymchak, Magnetic properties of the $CuCoAlBO_5$ single crystal, Physics of the Solid State 51 (2009) 2486.

[41] D. C. Freitas, R. B. Guimarães, J. C. Fernandes, M. A. Continentino, C. B. Pinheiro, J. A. L. C. Resende, G. G. Eslava, L. Ghivelder, Planar magnetic interactions in the hulsite-type oxyborate $Co_{5.52}Sb_{0.48}(O_2BO_3)_2$, Phys. Rev. B 81 (2010) 174403.

[42] N. B. Ivanova, M. S. Platunov, Y. V. Knyazev, N. V. Kazak, L. N. Bezmaternykh, E. V. Eremin, A. D. Vasiliev, Spin-glass magnetic ordering in $CoMgGaO_2BO_3$ ludwigite, Low Temperature Physics 38 (2012) 172.

[43] D. C. Freitas, R. B. Guimarães, D. R. Sanchez, J. C. Fernandes, M. A. Continentino, J. Ellena, A. Kitada, H. Kageyama, A. Matsuo, K. Kindo, G. G. Eslava, L. Ghivelder, Structural and magnetic properties of the oxyborate $Co_5Ti(O_2BO_3)_2$, Phys. Rev. B 81 (2010) 024432.

[44] Transition from quasi-one-dimensional to spin-glass behaviour in insulating $FeMg_2BO_5$, Journal of Magnetism and Magnetic Materials 173 (1997) 117.

[45] L. Bezmaternykh, E. Moshkina, E. Eremin, M. Molokeev, N. Volkov, Y. Seryotkin, Spin-Lattice Coupling and Peculiarities of Magnetic Behavior of Ferrimagnetic Ludwigites $Mn_{0.52}M_{1.52}Mn_3BO_5$ (M=Cu, Ni), Ch. Chapter 2: Magnetic Semiconductors and Oxides.

[46] R. Norrestam, K. Nielsen, I. Søtofte and N. Thorup, Structural investigation of two synthetic oxyborates: The mixed magnesium-manganese and the pure cobalt ludwigites, $Mg_{1.93}Mn_{1.07}O_2BO_3$ and $Co_3O_2BO_3$, Zeitschrift für Kristallographie - Crystalline Materials 189.

[47] Structural Characterizations of Two Synthetic Ni-Ludwigites, and Some Semiempirical {EHTB} Calculations on the Ludwigite Structure Type, Journal of Solid State Chemistry 111 (1994) 217.

[48] J. C. Fernandes, R. B. Guimarães, M. A. Continentino, H. A. Borges, A. Sulpice, J.-L. Tholence, J. L. Siqueira, L. I. Zawislak, J. B. M. da Cunha, C. A. dos Santos, Magnetic interactions in the ludwigite $Ni_2FeO_2BO_3$, Phys. Rev. B 58 (1998) 287.

[49] D. C. Freitas, M. A. Continentino, R. B. Guimarães, J. C. Fernandes, E. P. Oliveira, R. E. Santelli, J. Ellena, G. G. Eslava, L. Ghivelder, Partial magnetic ordering and crystal structure of the ludwigites $Co_2FeO_2BO_3$ and $Ni_2FeO_2BO_3$, Phys. Rev. B 79 (2009) 134437.

[50] Guimarães, R. B. and Mir, M. and Fernandes, J. C. and Continentino, M. A. and Borges, H. A. and Cernicchiaro, G. and Fontes, M. B. and Candela, D. R. S. and Baggio-Saitovitch, E., Cation-mediated interaction and weak ferromagnetism in $Fe_3O_2BO_3$, Phys. Rev. B 60 (1999) 6617.

Appendix A

Ludwigites till now

The table A.1 shows ludwigites that are being synthesized or found in nature and transition temperatures reported for these materials.

Table A.1: Table shows the chemical formula of ludwigites and transition temperatures T_N antiferromagnetic, T_C ferromagnetic/weak ferromagnetic, T_g spin glass

Chemical formula	Transition temperatures
$Fe_3O_2BO_3$	283K (Structural) [4], 112K (T_N), 70K (T_C), 40K (??) [5]
$Co_3O_2BO_3$	43K (T_{C1}), 15K (T_{C2}) [35]
$Ni_2FeO_2BO_3$	15K (T_N) [36]
$Co_{2.86}Fe_{0.14}O_2BO_3$	83K (T_{C1}), 74K (T_{C2}) [35]
$Co_{2.25}Fe_{0.75}O_2BO_3$	115K (T_N), 70K (T_C)[37]
$Mn_{1.2}Ni_{1.8}O_2BO_3$	92K (T_N) [32]
$Co_2FeO_2BO_3$	110K (T_N) [38]
$Co_{2.4}Ga_{0.6}O_2BO_3$	37K (T_C) [3]
$Cu_2FeO_2BO_3$	32K (T_N) [39]
$Cu_2GaO_2BO_3$	3.4K (T_N) [39]
$CuCoAlO_2BO_3$	28K (T_N) [40]
$Co_{5.2}Sb_{0.48}(O_2BO_3)_2$	42K (T_N)[41]
$CoMgGaO_2BO_3$	25K (T_g) [42]
$Co_5Ti(O_2BO_3)_2$	19K (T_g) [43]
$FeMg_2O_2BO_3$	8K (T_g) [44]
$Co_{2.1}Al_{0.9}O_2BO_3$ [18]	unreported
$Cu_2Al_2O_2BO_3$ [18]	unreported
$Mn_{1.5}M_{1.5}O_2BO_3$ M = Cu, Ni [45]	unreported
$Mg_{1.93}Mn_{1.37}O_2BO_3$ [46]	unreported
$Ni_2MO_2BO_3$ M = Cr, V [47]	unreported
$Ni_2MO_2BO_3$, M = Ga, Fe, Al, Cr [19]	unreported
$Ni_2AlO_2BO_3$	38K (T_N) (present work)
$Co_2AlO_2BO_3$	36K (T_N) (present work)

Appendix B

Trials for synthesis of other Ludwigites

During my project I have tried synthesizing other ludwigites especially $Ni_2FeO_2BO_3$ and $Fe_2FeO_2BO_3$.

B.1 Trials for synthesis of $Ni_2FeO_2BO_3$

There were in total eight trials done for synthesizing pure phase of $Ni_2FeO_2BO_3$. The first three trials were done using alumina crucibles,fourth and fifth trials using Nickel crucibles and last three were using platinum crucible.

- Trial 1 & 2 Alumina crucible was used with NiO and Fe_2O_3 were taken in stoichiometric ratio with borax as flux fired at 1050^oC in reference to J. C. Fernandes *et.al* [48]. The reactions did not yield any trace of $Ni_2FeO_2BO_3$.

- Third trial instead of Borax, boric acid was used as flux in reference to Freitas *et.al* [49].

- Nickel crucibles were used in fourth and fifth trials and the reaction temperature was kept at 1000^oC and 1300^oC respectively. Both of them had NiO phase because of the oxidation of Nickel crucible.

- In the last three trials platinum crucible was used for the reaction which was carried out at 1300^oC with varying amount of flux (Borax). Interestingly there was a phase of $Ni_2FeO_2BO_3$ but with an additional major phase of NiO. NiO phase did not seem to reduce in any of the last three trials.

B.2 Trials for synthesis of $Fe_3O_2BO_3$

The reaction was done according to Guimarães, R. B. *et.al* [50] in which "Fe sample was prepared by heating at 1120^{o}C a stoichiometric mixture of FeO, Fe_2O_3, and B_2O_3 in borax under an argon atmosphere" [50]. The first reaction was done without FeO due to its unavailability. While the second reaction was done excatly as mentioned Guimarães, R. B. *et.al* [50] in an alumina crucible. However in both the reactions, the crucible was reacting to the sample giving rise to other borate phases.